

## Original Article

**Cite this article:** Bhat IM, Ahmad T, Rao DVS, and Rao NVC (2021) Petrological and geochemical characterization of the arc-related Suru–Thasgam ophiolitic slice along the Indus Suture Zone, Ladakh Himalaya. *Geological Magazine* 158: 1441–1460. <https://doi.org/10.1017/S0016756821000042>


Received: 7 October 2020  
Accepted: 8 January 2021  
First published online: 10 February 2021

**Keywords:**

pyroxenites; peridotites; geochemistry; ophiolites; western Ladakh

**Author for correspondence:** I.M. Bhat,  
Email: [imbhat89@gmail.com](mailto:imbhat89@gmail.com)

# Petrological and geochemical characterization of the arc-related Suru–Thasgam ophiolitic slice along the Indus Suture Zone, Ladakh Himalaya

I.M. Bhat<sup>1</sup> , T. Ahmad<sup>2</sup>, D.V. Subba Rao<sup>3</sup> and N.V. Chalapathi Rao<sup>4</sup>

<sup>1</sup>Department of Earth Sciences, University of Kashmir, Srinagar-190006, India; <sup>2</sup>Vice Chancellors Office, University of Kashmir, Srinagar-190006, India; <sup>3</sup>Geochemistry Division, National Geophysical Research Institute (NGRI), Hyderabad-500606, India and <sup>4</sup>Centre of Advanced Study in Geology, Institute of Science, Banaras Hindu University, Varanasi-221005, India

**Abstract**

The Ladakh Himalayan ophiolites preserve remnants of the eastern part of the Neo-Tethyan Ocean, in the form of Dras, Suru Valley, Shergol, Spongtag and Nidar ophiolitic sequences. In Kohistan region of Pakistan, Muslim Bagh, Zhob and Bela ophiolites are considered to be equivalents of Ladakh ophiolites. In western Ladakh, the Suru–Thasgam ophiolitic slice is highly dismembered and consists of peridotites, pyroxenites and gabbros, emplaced as imbricate blocks thrust over the Mesozoic Dras arc complex along the Indus Suture Zone. The Thasgam peridotites are partially serpentinized with relict olivine, orthopyroxene and minor clinopyroxene, as well as serpentine and iron oxide as secondary mineral assemblage. The pyroxenites are dominated by clinopyroxene followed by orthopyroxene with subordinate olivine and spinel. Gabbros are composed of plagioclase and pyroxene (mostly replaced by amphiboles), describing an ophitic to sub-ophitic textural relationship. Geochemically, the studied rock types show sub-alkaline tholeiitic characteristics. The peridotites display nearly flat chondrite-normalized rare earth element (REE) patterns ( $(La/Yb)_N = 0.6–1.5$ ), while fractionated patterns were observed for pyroxenites and gabbros. Multi-element spidergrams for peridotites, pyroxenites and gabbros display subduction-related geochemical characteristics such as enriched large-ion lithophile element (LILE) and depleted high-field-strength element (HFSE) concentrations. In peridotites and pyroxenites, highly magnesian olivine ( $Fo_{88.5-89.3}$  and  $Fo_{87.8-89.9}$ , respectively) and clinopyroxene (Mg no. of 93–98 and 90–97, respectively) indicate supra-subduction zone (SSZ) tectonic affinity. Our study suggests that the peridotites epitomize the refractory nature of their protoliths and were later evolved in a subduction environment. Pyroxenites and gabbros appear to be related to the base of the modern intra-oceanic island-arc tholeiitic sequence.

**1. Introduction**

The palaeo-oceanic lithosphere is emplaced along the convergent plate boundaries in the form of ophiolite complexes, which originated either at mid-ocean ridges (MOR) or supra-subduction zones (SSZ) including fore-arc/back-arc regions (Dilek & Newcomb, 2003; Dilek & Furnes, 2009, 2014; Pearce, 2014). Ophiolites are reported from different parts of the globe along the orogenic belts ranging in age from Archean to Cenozoic with MOR and SSZ geochemical characteristics (Dilek & Robinson, 2003). The ophiolites of Proterozoic age (870–627 Ma) occur in the Arabian Shield and in the Atlas Mountains in NW Africa, while the Mesozoic–Cenozoic ophiolites are distributed along the Alpine–Himalayan Orogenic Belt and in the Philippines (Furnes *et al.* 2020). The geodynamic scenario of most of the global ophiolite sequences remains contentious with two competing tectonic settings: a MOR setting (Coleman, 1977) and an SSZ setting (Pearce, 2014; Hodel *et al.* 2020). However, both the MORB and SSZ geochemical affinities often co-exist within the same ophiolite, for example, Mirdita ophiolite, Albania (Dilek *et al.* 2008) and other Tethyan ophiolites (Dilek & Furnes, 2019).

Well-studied Mesozoic Neo-Tethyan ophiolitic sequences are exposed along the northern Indian plate margin, that is, Indus Yarlung Tsangbo Suture (IYTS; Hebert *et al.* 2012; Liu *et al.* 2016; Bhat *et al.* 2017a, 2019a, b; Kingson *et al.* 2017; Xiong *et al.* 2017; Buckman *et al.* 2018; Jadoon *et al.* 2020). However, due to extreme high altitude (average height 3000 m) and poor accessibility to the Ladakh terrain, especially Kargil region of western Ladakh, limited research work has been carried out on the western Ladakh ophiolites, particularly on Suru–Thasgam dismembered ophiolitic slice, thrust over the Dras arc complex. Here we report for the first time the petrological and geochemical characteristics of mafic–ultramafic rocks of the Suru–Thasgam ophiolitic slice. Our study is an attempt to understand

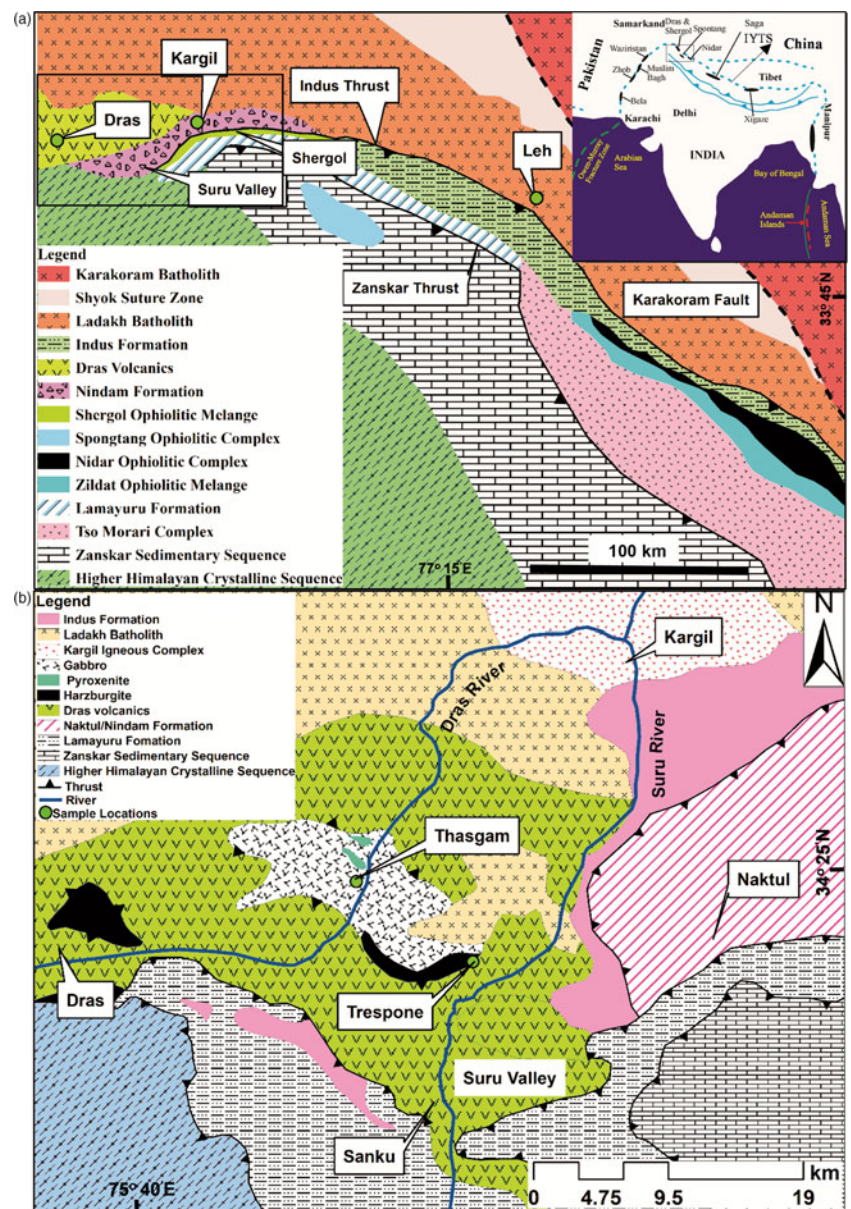


**Fig. 1.** (Colour online) (a) Geological map of the Ladakh Himalaya (modified after Maheo *et al.* 2004) showing the location of the study area (rectangle) and with an inset map of the Himalayan–Tibetan Orogen (modified after Dilek & Furnes, 2009). (b) Detailed geological map of the Kargil District of Ladakh Himalaya (modified after Reuber, 1989) showing the Suru–Thasgam ophiolitic slice.

the petrogenesis and to correlate and compare this with other Neo-Tethyan ophiolites, based on integrated mineralogical and geochemical datasets.

## 2. Regional geology

Ophiolites of Mesozoic age are exposed along the IYTS (Fig. 1a) and represent remnants of the eastern portion of the Neo-Tethyan Ocean (Maheo *et al.* 2004; Ahmad *et al.* 2008; Dilek & Furnes, 2009, 2011, 2019; Aitchison *et al.* 2011; Bhat *et al.* 2017a, 2019a, b; Buckman *et al.* 2018). In Ladakh Himalaya (Fig. 1a), the ophiolitic slices from NW to SE are: Dras ophiolitic slice (Radhakrishna *et al.* 1984, 1987); Suru Valley ophiolitic slice (Robertson, 2000; Bhat *et al.* 2019b); Shergol ophiolitic slice (Bhat *et al.* 2017a, b, 2019c); Spong tang ophiolite complex (Maheo *et al.* 2004); and Nidar ophiolitic complex (Ahmad *et al.* 1996, 2008). These ophiolites are highly dismembered, similar to other Tethyan ophiolites (Moores *et al.* 2000), and are emplaced as imbricate blocks thrust over the Mesozoic Dras arc complex comprising Dras volcanics

and Nindam/Naktul Formations (Honegger *et al.* 1982; Radhakrishna *et al.* 1984; Reuber, 1989; Robertson, 2000; Maheo *et al.* 2006; Bhat *et al.* 2017a, 2019a, b). Earlier workers suggested that these rootless sub-horizontal bodies of ophiolites from Ladakh Himalaya represent substratum of the Dras arc complex (e.g. Reuber, 1989; Robertson, 2000). Many others argued for their origin at palaeo-MOR in the context of the Neo-Tethys Ocean, emplaced during Late Cretaceous time along the Indus Suture Zone (ISZ) (e.g. Brookfield & Reynolds, 1981; Radhakrishna *et al.* 1984; Reuber *et al.* 1990). However, recent work based on the detailed whole-rock, mineral and isotope data proposed that these ophiolitic slices were evolved in a SSZ tectonic setting in the context of the Neo-Tethys Ocean (Maheo *et al.* 2004; Ahmad *et al.* 2008; Bhat *et al.* 2017a, 2019a, b, 2021; Buckman *et al.* 2018; Jonnalagadda *et al.* 2019).

The Dras arc complex, a dominant tectonic unit in the study area (Fig. 1b), represents part of the intra-oceanic arc formed within the Neo-Tethyan Ocean during the Cretaceous Period above an inferred N-dipping subduction zone. It dominantly

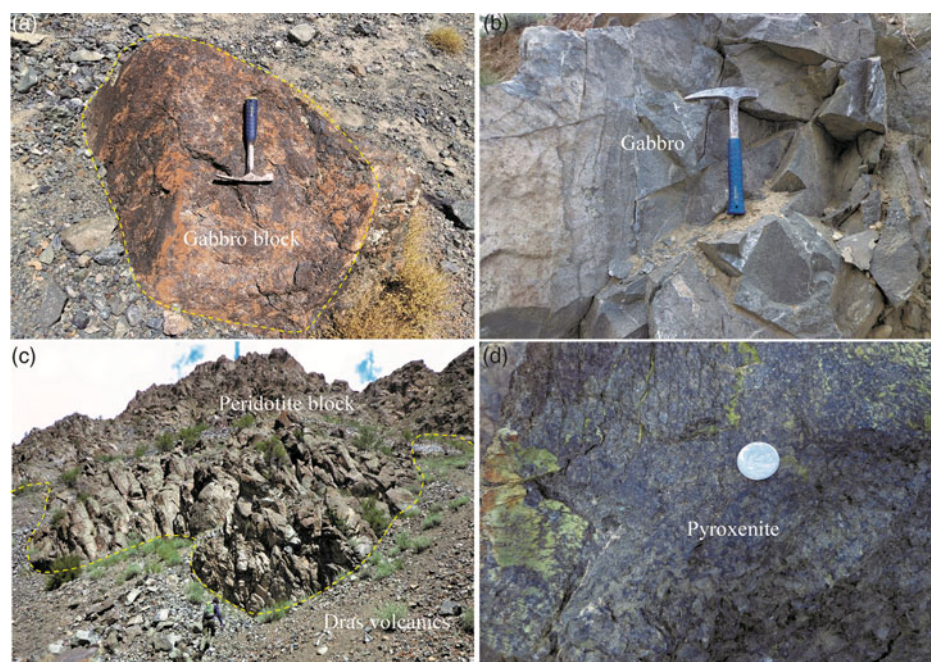


**Fig. 2.** (Colour online) Field photographs of (a) isolated massive gabbro block at Trespone Village of Suru Valley; (b) outcrop of fresh gabbro near Thasgam Village; (c) peridotite block at Trespone Village; and (d) well-exposed pyroxenite at Thasgam Village of Dras.

comprises mafic to intermediate volcanics with subordinate shallow- to deep-marine volcano-sedimentary assemblage of fore-arc apron known as the Nindam Formation (Robertson & Degnan, 1994; Robertson, 2000). This arc complex is overlain by dismembered Late Jurassic Neo-Tethyan oceanic lithosphere (Reuber, 1989; Robertson, 2000). According to Reuber (1989), part of this oceanic lithosphere, comprising serpentinized peridotites (Suru Valley Peridotites of Bhat *et al.* 2019b) with minor gabbros, best exposed in the Suru Valley, represents tectonically disrupted oceanic substratum of the Cretaceous Dras arc complex. Based on mineral and whole-rock geochemistry, Bhat *et al.* (2019b) recently suggested that these peridotites evolved in an intra-oceanic subduction environment corresponding to Dras arc complex.

### 3. Field relationships

The Suru–Thasgam dismembered ophiolitic slice is composed of serpentinized peridotites, pyroxenites and gabbros thrust over the Dras arc complex as isolated blocks (Fig. 1b). Robertson & Degnan (1994) classified the Dras arc complex into three structural units from west to east: the Suru Formation (arc interior dominated by Dras volcanics), the Naktul Formation (a shallow-water fore-arc apron comprising thickly bedded turbidites and carbonates) and the Nindam Formation (a deep-water fore-arc apron comprising volcanoclastic turbidites and pelagic carbonates). This NW–SE-striking ophiolitic slice extends between Thasgam and Trespone villages towards SW of Kargil town, measuring *c.* 20 km in length and 10–12 km in width (Fig. 1b). Its southeastern exposure is marked by the Suru River where the gabbros and peridotites are exposed on the river bank. The Dras River flows through this ophiolitic slice at Trespone village, and the ophiolitic rocks such as gabbros and pyroxenites crop out along the Dras–Kargil National Highway on both banks of the river. The contact between the ophiolitic slice and underlying Dras volcanics is faulted as evident in the field and also described by earlier workers (e.g. Radhakrishna *et al.* 1984, 1987; Robertson, 2000; Bhat *et al.* 2019b). The sampled outcrops of the Suru–Thasgam ophiolitic

slice are depicted in Figure 2 and their geographic coordinates are provided in Tables 1 and 2.

The medium- to coarse-grained dark-green-coloured massive gabbros are exposed as isolated blocks (1–4 m across) at the Trespone Village in Suru Valley (Fig. 2a), and also along the opposite banks of the Dras River near Thasgam Village (Fig. 2b). Gabbro samples SM2–6 were collected from Trespone Village and SM10–15 were collected from the Thasgam Village (respective coordinates provided in Table 2). These dark-green-coloured gabbros comprise the dominant component of the dismembered ophiolite suite of the study area. The isolated peridotite block, up to 100 m across, is exposed at Trespone Village towards the left bank of the downstream Suru River, overlying the Dras volcanics (Fig. 2c). Here black- to dark-green-coloured peridotite samples DP3–5 (coordinates provided in Table 1) were collected. In addition, undeformed cumulate textured pyroxenite blocks (Fig. 2d) are exposed at Thasgam Village along the left bank of downstream Dras River adjacent to gabbros. Olive-green-coloured pyroxenite samples TG10–15 (coordinates provided in Table 1) were collected from an isolated block on the road side.

### 4. Petrography

We conducted out petrographic study on 36 mafic–ultramafic rock samples from the Suru–Thasgam ophiolitic slice, described in detail in the following sections.

#### 4.a. Peridotites

The peridotites are dominantly composed of variable sizes (0.2–0.5 mm across) of olivine (50–60 modal %), < 1 mm across orthopyroxene (20–30 modal %) with < 0.5 mm across clinopyroxene (5–10 modal %) and < 0.4 mm across spinel grains (< 5 modal %). Oxides and serpentine (< 10 modal %) are present as secondary mineral assemblages, whereby olivine has occasionally transformed into serpentine (Fig. 3a) reflecting the low degree of serpentinization (< 10%). Clinopyroxene was absent from sample DP3. The samples are therefore compositionally similar

**Table 1.** Major (wt%) and trace (ppm) element peridotite and pyroxenite data from the Suru–Thasgam ophiolitic slice, western Ladakh

Sample no.	Peridotites			Pyroxenites					
	DP3	DP4	DP5	TG11	TG12	TG13	TG14	TG15	TG10
Latitude (N)	34° 23' 19"	34° 23' 33"	34° 24' 06"	34° 29' 20"	34° 29' 18"	34° 29' 13"	34° 29' 10"	34° 29' 06"	34° 28' 58"
Longitude (E)	75° 58' 05"	75° 58' 25"	75° 58' 18"	75° 56' 25"	75° 56' 22"	75° 56' 18"	75° 55' 04"	75° 55' 10"	75° 55' 25"
Major oxides (wt%)									
SiO <sub>2</sub>	41.5	40.4	40.1	42.9	48.5	47.4	50.2	50.9	45.9
TiO <sub>2</sub>	0.10	0.12	0.14	0.94	0.05	0.06	0.04	0.07	0.14
Al <sub>2</sub> O <sub>3</sub>	2.16	2.20	2.81	5.80	2.27	2.36	2.26	2.46	4.07
Fe <sub>2</sub> O <sub>3t</sub>	10.03	9.70	11.20	10.78	8.99	8.68	8.07	9.15	13.80
MnO	0.14	0.14	0.12	0.14	0.07	0.07	0.09	0.07	0.08
MgO	41.25	42.43	40.87	21.23	18.87	22.24	20.30	17.71	20.53
CaO	1.53	1.38	1.33	17.38	21.19	19.11	18.93	19.46	12.79
Na <sub>2</sub> O	0.22	0.22	0.50	0.54	0.06	0.06	0.03	0.05	0.38
K <sub>2</sub> O	0.03	0.04	0.06	0.20	0.01	0.01	0.01	0.01	0.04
P <sub>2</sub> O <sub>5</sub>	0.04	0.04	0.05	0.08	0.02	0.02	0.02	0.02	0.03
LOI	3.40	4.20	3.70	0.02	0.03	0.01	0.02	0.01	0.20
Sum	100.4	100.8	100.7	100.02	100.03	100.01	100.02	100.01	100.01
Mg no.	90	90	89	81	82	84	84	80	76
Trace elements (ppm)									
Sc	22	22	92	131	45	71	40	75	11
V	109	120	193	371	111	177	182	84	51
Cr	3367	4025	2564	1512	3368	4385	2599	4408	7374
Co	164	147	73	62	48	58	92	66	151
Ni	3230	2901	2565	220	294	348	543	345	299
Cu	29	47	22	266	110	136	119	125	142
Zn	72	106	35	176	78	85	117	57	130
Ga	4.2	4.8	3.3	15.7	13.8	31.1	39.1	4.5	6.1
Cs	0.21	0.19	0.18	0.52	1.77	3.9	4.34	0.61	0.58
Rb	1.67	1.78	1.22	10.9	9.79	12.6	11.4	10.9	10.5
Ba	34	16	9	52	71	154	177	27	26
Sr	11	12	11	101	50	70	80	34	15
Y	3.9	3.9	4.3	30	10	18	25	3.6	2.3

(Continued)

**Table 1.** (Continued)

Zr	11	9	9	73	27	96	45	82	51
Hf	0.29	0.25	0.23	2.35	16.18	28.97	40.80	2.49	3.10
Nb	0.12	0.08	0.06	1.31	2.40	3.85	5.29	0.51	1.41
Ta	0.06	0.08	0.44	0.32	0.54	0.92	1.00	0.09	0.55
Pb	23	12	4	14	14	24	24	9	10
Th	0.25	0.16	0.38	0.68	1.79	3.59	4.36	0.40	0.50
U	0.09	0.06	0.09	0.19	1.16	2.16	2.84	0.20	0.24
Rare earth elements (ppm)									
La	0.52	0.38	0.89	4.14	6.87	14.04	16.90	1.67	1.92
Ce	0.87	0.71	1.31	11.24	12.57	26.13	32.38	3.16	3.55
Pr	0.19	0.15	0.28	1.88	1.36	2.75	3.21	0.37	0.38
Nd	0.87	0.78	1.29	11.62	5.47	11.00	12.59	1.76	1.50
Sm	0.29	0.26	0.38	3.67	1.31	2.61	2.89	0.53	0.34
Eu	0.11	0.11	0.14	1.36	0.28	0.52	0.59	0.14	0.09
Gd	0.44	0.42	0.60	4.79	1.23	2.31	2.75	0.51	0.30
Tb	0.08	0.09	0.12	0.80	0.22	0.39	0.48	0.09	0.05
Dy	0.57	0.58	0.76	4.87	1.38	2.40	3.04	0.54	0.29
Ho	0.14	0.14	0.16	0.95	0.30	0.53	0.67	0.11	0.07
Er	0.44	0.45	0.47	2.25	0.85	1.48	1.93	0.28	0.18
Tm	0.08	0.08	0.08	0.27	0.13	0.22	0.29	0.04	0.03
Yb	0.47	0.49	0.43	1.51	0.87	1.55	2.10	0.23	0.19
Lu	0.07	0.07	0.06	0.18	0.13	0.23	0.31	0.03	0.03

**Table 2.** Major (wt%) and trace (ppm) element gabbro data from the Suru–Thasgam ophiolitic slice, western Ladakh. ND – not defined.

Sample no.	SM2	SM3	SM4	SM5	SM6	SM10	SM11	SM12	SM13	SM14	SM15
Latitude (N)	34° 25' 36"	34° 25' 21"	34° 25' 05"	34° 24' 25"	34° 24' 10"	34° 28' 57"	34° 28' 34"	34° 28' 16"	34° 27' 56"	34° 27' 29"	34° 26' 12"
Longitude (E)	76° 04' 48"	76° 02' 03"	76° 00' 45"	75° 59' 36"	76° 58' 43"	75° 56' 58"	75° 56' 14"	75° 55' 49"	75° 55' 40"	75° 55' 12"	75° 55' 02"
SiO <sub>2</sub>	48.6	51.1	49.8	50.5	52.0	51.6	50.3	47.9	51.1	46.9	50.5
TiO <sub>2</sub>	1.63	1.39	0.89	0.13	1.11	0.76	0.87	0.43	0.76	0.67	1.04
Al <sub>2</sub> O <sub>3</sub>	13.5	14.8	15.2	13.5	14.7	12.6	15.1	15.9	15.5	15.2	14.8
Fe <sub>2</sub> O <sub>3t</sub>	12.8	12.1	9.3	11.5	13.3	10.9	10.3	10.3	10.6	12.6	11.2
MnO	0.14	0.14	0.12	0.16	0.13	0.19	0.16	0.11	0.16	0.15	0.14
MgO	8.15	7.80	8.82	10.81	7.90	10.75	9.99	10.68	8.61	9.15	9.02
CaO	11.13	9.22	12.98	12.74	6.98	10.07	9.99	12.66	10.19	13.63	8.32
Na <sub>2</sub> O	2.44	2.58	1.51	0.35	3.16	2.14	1.55	0.72	2.39	1.27	2.36
K <sub>2</sub> O	0.20	0.27	0.20	0.05	0.11	0.31	0.41	0.06	0.31	0.44	0.55
P <sub>2</sub> O <sub>5</sub>	0.18	0.14	0.09	0.03	0.09	0.15	0.08	0.04	0.07	0.09	0.14
LOI	1.33	1.39	1.19	0.30	2.01	1.03	1.99	1.63	0.94	0.74	2.73
Sum	100.2	100.9	100	100.1	101.5	100	100.7	100.4	100.7	100.9	100.7
Mg no.	57	58	67	66	56	68	67	69	63	61	63
CaO/Al <sub>2</sub> O <sub>3</sub>	0.8	0.6	0.8	1.1	0.5	1.05	0.6	0.95	0.7	0.9	0.6
Trace elements (ppm)											
Sc	66	52	35	ND	57	47	42	62	56	72	56
V	370	331	216	–	358	328	272	200	292	381	314
Cr	300	286	190	–	69	441	582	263	496	511	369
Co	45	31	30	–	33	48	41	35	36	49	42
Ni	165	155	78	–	67	205	189	163	152	166	159
Cu	164	163	134	–	142	12	110	139	133	211	150
Zn	114	112	71	–	111	51	110	132	116	208	107
Ga	27	23	12	–	21	15	13	20	16	26	26
Cs	0.7	1.1	0.3	–	0.5	0.5	0.7	0.9	0.8	1.6	1.3
Rb	11.1	9.5	7.3	–	9.9	6.4	9.9	9.4	9.9	12.2	14.7
Ba	117	109	44	–	48	28	61	44	64	153	275
Sr	332	213	155	–	171	127	125	166	165	233	255
Y	41	29	16	–	27	16	20	12	19	20	32
Zr	150	188	52	–	76	18	132	175	94	387	255

(Continued)

**Table 2.** (Continued)

Hf	4.52	5.74	1.67	–	2.42	0.51	4.13	5.25	2.98	11.52	7.30
Nb	5.28	2.79	0.85	–	1.27	0.22	1.71	0.78	0.85	2.06	3.26
Ta	0.34	0.28	0.15	–	0.14	0.11	0.50	0.17	0.17	0.31	0.34
Pb	9.8	12.1	7.1	–	8.2	6.4	9.4	15.1	10.1	24.6	12.3
Th	1.01	1.35	0.56	–	0.82	0.36	0.97	0.93	0.68	1.89	1.58
U	0.33	0.43	0.14	–	0.19	0.10	0.30	0.40	0.23	0.92	0.53
Rare earth elements (ppm)											
La	10.5	8.8	3.4	–	5.5	1.8	5.7	3.9	3.8	10.2	9.2
Ce	25.7	19.7	7.9	–	13.5	3.6	12.5	7.5	8.8	22.1	20.8
Pr	3.52	2.51	1.03	–	1.81	0.87	1.60	0.91	1.18	2.39	2.6
Nd	17.5	12.3	5.3	–	9.7	4.5	7.8	4.4	6.2	10.5	12.8
Sm	5.54	3.86	1.75	–	3.31	1.40	2.44	1.39	2.11	2.90	4.00
Eu	1.99	1.35	0.68	–	1.19	0.61	0.78	0.58	0.78	0.81	1.32
Gd	6.24	4.20	2.06	–	3.76	1.95	2.74	1.59	2.57	2.85	4.36
Tb	1.04	0.72	0.36	–	0.65	0.37	0.47	0.28	0.45	0.48	0.75
Dy	6.30	4.50	2.35	–	4.14	2.51	3.01	1.76	2.94	2.90	4.73
Ho	1.26	0.91	0.49	–	0.85	0.55	0.63	0.38	0.61	0.61	0.98
Er	2.97	2.22	1.18	–	2.06	1.73	1.55	0.95	1.49	1.56	2.38
Tm	0.36	0.28	0.15	–	0.26	0.27	0.20	0.12	0.19	0.21	0.30
Yb	2.05	1.66	0.85	–	1.50	1.76	1.18	0.73	1.11	1.30	1.80
Lu	0.24	0.22	0.11	–	0.21	0.24	0.15	0.10	0.15	0.19	0.23

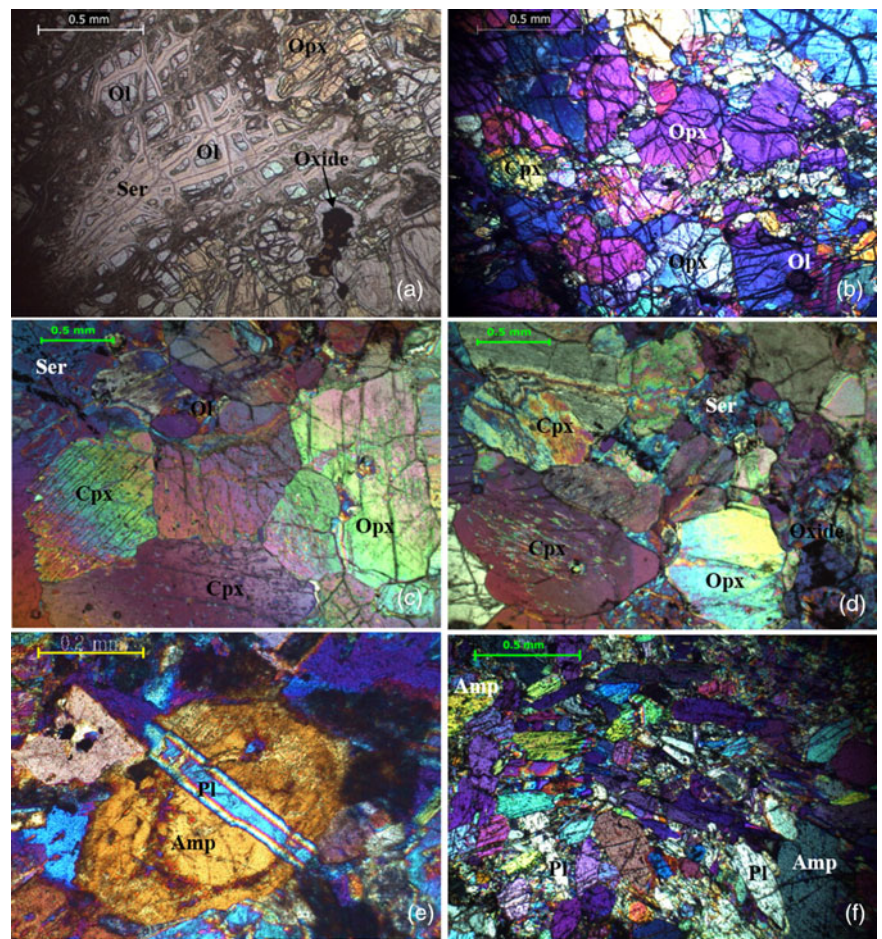


**Fig. 3.** (Colour online) Photomicrographs under crossed-polarized light: (a) peridotite with variable sizes of mineral grains; (b) peridotite showing proto-granular texture; (c) pyroxenite with cumulate texture; (d) pyroxenite with intercumulus space occupied by olivine grains; (e) gabbro with zoned plagioclase (Pl) in amphibole (Amp) after clinopyroxene; and (f) gabbro with ophitic to sub-ophitic textural relationship of mineral grains.

to clinopyroxene-absent and clinopyroxene-bearing spinel harzburgites. They also exhibit deformational features such as undulatory extinction and kink bands, reflecting their tectonite nature. These rock types have smoothly curved olivine crystals with proto-granular texture (Fig. 3b), and serpentine veins cut across the olivine and orthopyroxene crystals in places. Dark-brown vermicular spinel grains (< 0.4 mm across), commonly altered to iron oxides, also occur along margins and fractures between the silicate minerals.

#### 4.b. Pyroxenites

Petrographically, this rock type has a cumulate nature with composition ranging from olivine websterite to clinopyroxenite. The studied pyroxenites are distinguished from the peridotites based on their colour, textural features and mineralogical composition. The primary mineral assemblage constitutes clinopyroxene (Cpx; 60–70 modal %), orthopyroxene (Opx; 10–20 modal %), olivine (Ol; 5–10 modal %) and spinel (< 5 modal %); minor serpentine (Ser; < 3 modal %) and iron oxides constitute the secondary mineral assemblage. At places, the inter-cumulus spaces are occupied by small- to medium-grained olivine in the majority of the cases, and sometimes (rarely) by reddish-brown spinel grains. This rock type displays no evidence of deformation and therefore preserves the primary textures of a cumulate rock type (Fig. 3c). Both the pyroxene types occur in the form of subhedral grains (0.5–1.5 mm across) with a dominance of clinopyroxene in most samples. Small euhedral–subhedral olivine grains occur as

inclusions in pyroxene grains and, at places, exhibit triple junctions along with orthopyroxene and clinopyroxene grains at intercumulus spaces (Fig. 3d). Secondary serpentine and iron oxide (< 0.5 mm across) are observed within the cracks and along grain boundaries of olivine and pyroxene. Small euhedral–subhedral grains of reddish-brown spinel (< 0.5 mm across) are present and are partially or totally included in the associated silicate minerals, indicating their early crystallization.

#### 4.c. Gabbros

Gabbros are essentially composed of medium-grained plagioclase (65 modal %) and amphibole grains (20 modal %) with < 15 modal % of clinopyroxene, chlorite and iron oxide. At places, plagioclase feldspars show zoning and partial alteration to saussurite. Clinopyroxenes are replaced by amphiboles (Fig. 3e), while iron oxide occurs mostly along the margins of amphiboles. This rock type shows an ophitic to sub-ophitic textural relationship of mineral grains, with a few samples having a hypidiomorphic texture (Fig. 3f).

## 5. Geochemistry

### 5.a. Analytical techniques

After careful petrographic study, relatively fresh representative samples of peridotites (3 samples), pyroxenites (6 samples) and gabbros (11 samples) from the Suru–Thasgam ophiolitic slice were selected for geochemical analysis. The samples were crushed into



small chips to remove the weathered parts. These rocks were then manually pulverized/milled using an agate mortar and pestle. Loss on ignition (LOI) was determined by heating a separate aliquot of sample powder (5 g) at 950°C. The whole-rock major-oxide analysis was carried out on powder pellets using an X-ray fluorescence spectrometer (Philips Magi X PRO, Model PW 2440 wavelength-dispersive X-ray fluorescence spectrometer or WDXRF), coupled with an automatic sample changer. Trace elements including rare earth elements (REE) were analysed by wet chemical method using a high-resolution inductively couple plasma mass spectrometer (HRICP-MS) in jump-wiggle mode at moderate resolution of 300. The analytical procedures for major- and trace-element determination were as described by Krishna *et al.* (2007) and Satyanarayanan *et al.* (2014), respectively. All the analysis was performed at the National Geophysical Research Institute (NGRI), Hyderabad, India. Standard reference materials for mafic rock were BHVO-1 (USGS international basalt standard) and MRG-1 (Mount Royal Gabbro, Canada), and for peridotite PCC-1 (USGS international peridotite standard) and UBN were used along with a couple of procedural blanks. Analytical precision (relative standard deviation) for major elements is well below 1–2% for all the samples including reference standards and 3–5% for the majority of trace elements. The analytical results therefore demonstrate a high degree of machine accuracy and precision. Whole-rock major- (in wt%) and trace- (in ppm) element data of peridotites and pyroxenites are presented in Table 1, and that for gabbros in Table 2.

Mineral chemical analyses of olivine, orthopyroxene, clinopyroxene, plagioclase, amphibole and spinel from selected rock samples were performed at the BHU, Varanasi, using the electron probe microanalyser (EPMA) CAMECA SX-Five instrument. The instrument was operated at an acceleration voltage of 15 kV and probe current of 20 nA. Well-calibrated natural silicates were used as standards, and replicate analyses of individual points show an analytical error of < 2%. EPMA results of studied minerals are presented in online Supplementary Tables S1–S6 (available at <http://journals.cambridge.org/geo>).

## 5.b. Mineral chemistry

### 5.b.1. Olivine

Representative analyses of olivine from the peridotites and pyroxenites are presented in online Supplementary Table S1. The olivines in peridotite have relatively uniform composition. The forsterite content of olivine ranges from Fo<sub>88.5</sub> to Fo<sub>89.3</sub> in peridotites (typical range of mantle peridotites is Fo<sub>88–91</sub>, after Jonnalagadda *et al.* 2019) and from Fo<sub>87.8</sub> to Fo<sub>89.9</sub> in pyroxenites. MgO in peridotites ranges over 47.4–48.8 wt% and is almost similar to that of pyroxenites (47.6–48.6 wt%), whereas Cr<sub>2</sub>O<sub>3</sub> content increases from peridotites (i.e. 0.01–0.03 wt%) to pyroxenites (i.e. 0.03–0.15 wt%).

### 5.b.2. Orthopyroxene

Orthopyroxenes are abundant in peridotites; however, they are less abundant in pyroxenites and almost absent in gabbros. Representative analyses of orthopyroxene from peridotites are listed in online Supplementary Table S2. The orthopyroxene in peridotites is of enstatite composition varying from En<sub>86.9</sub> Fs<sub>9.4</sub> Wo<sub>1.3</sub> to En<sub>89.2</sub> Fs<sub>10.3</sub> Wo<sub>2.7</sub> (Fig. 4a). They are unzoned and highly magnesian with Mg no. ( $100 \times \text{Mg}^{2+}/(\text{Mg}^{2+} + \text{Fe}^{2+})$ ) ranging from 89 to 92. Further, they are characterized by higher Al<sub>2</sub>O<sub>3</sub> (4.9–5.5 wt%) and Cr<sub>2</sub>O<sub>3</sub> (0.52–0.57 wt%), and lower TiO<sub>2</sub> concentration (< 0.13 wt%).

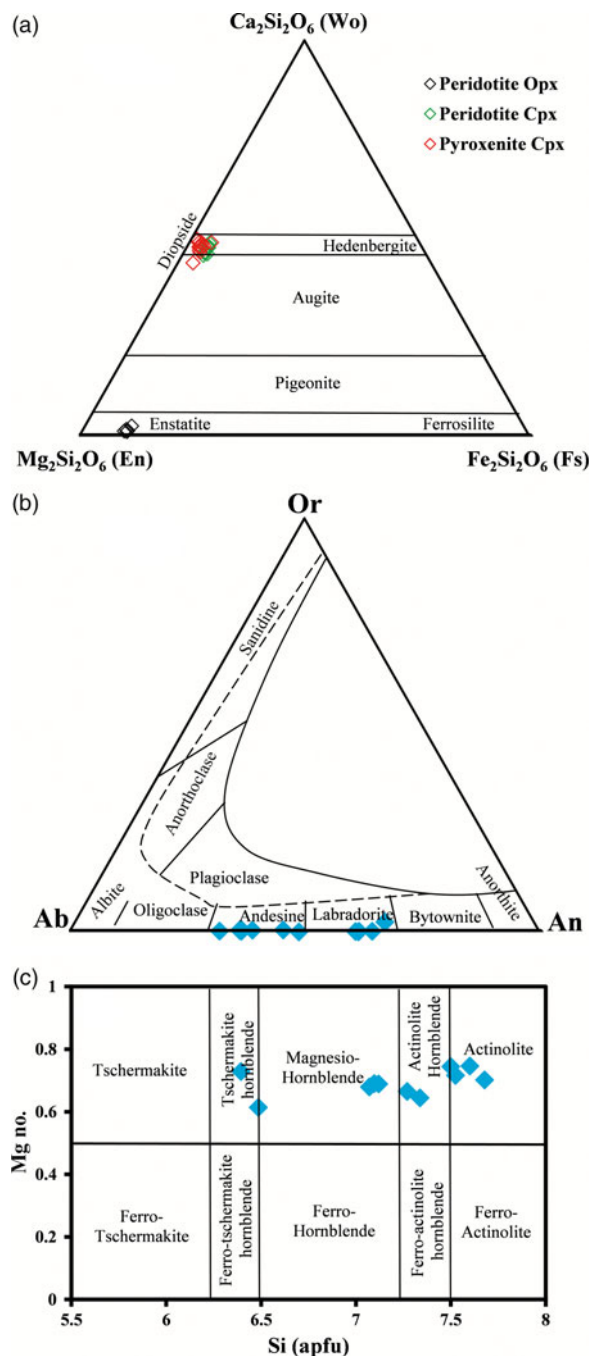


Fig. 4. (Colour online) Plots of (a) chemical variability of pyroxenes from peridotites and pyroxenites shown in Wollastonite–Enstatite–Ferrosilite pyroxene ternary classification diagram after Morimoto *et al.* (1989); (b) chemical variability of plagioclase from gabbros in Ab–An–Or feldspar ternary classification diagram after Deer *et al.* (1992); and (c) chemical composition of amphibole from gabbros in the Leake (1978) classification diagram.

### 5.b.3. Clinopyroxene

Representative analyses of clinopyroxenes from peridotites are listed in online Supplementary Table S2 and of pyroxenites in online Supplementary Table S3. The studied clinopyroxenes do not show any zoning in the studied rock types. The clinopyroxene in the peridotites have relatively uniform composition of En<sub>47–50</sub> Fe<sub>5–6</sub> Wo<sub>46–49</sub>, and on the wollastonite–enstatite–ferrosilite ternary diagram of Morimoto *et al.* (1989) they plot in the diopside field (Fig. 4a). The Mg no. (93–98) along with

Al<sub>2</sub>O<sub>3</sub>, CaO, Cr<sub>2</sub>O<sub>3</sub> and TiO<sub>2</sub> contents of the analysed clinopyroxenes range over 1.65–6.75 wt%, 21.02–24.5 wt%, 0.34–1 wt% and 0.1–0.49 wt%, respectively. In addition, the clinopyroxenes in pyroxenites are of diopside composition, that is, Wo<sub>44–50</sub> En<sub>46–53</sub> Fs<sub>1–5</sub> (Fig. 4a) with high Mg no. (93–97). Their Al<sub>2</sub>O<sub>3</sub>, Cr<sub>2</sub>O<sub>3</sub>, CaO and TiO<sub>2</sub> contents range over 0.39–2.26 wt%, 0.03–0.54 wt%, 22.01–25.16 wt% and 0.03–0.15 wt%, respectively.

#### 5.b.4. Spinel

Representative analyses of spinel from the pyroxenites is shown in online Supplementary Table S4. The studied spinels are Cr-rich (52.2–40.1 wt%) and Al depleted (7.4–14.2 wt%). They show a wide compositional range with high Cr no. ( $100 \times \text{Cr}^{3+}/(\text{Cr}^{3+} + \text{Al}^{3+} + \text{Fe}^{3+})$ ) of 54–72 and low Mg no. of 27–40 (online Supplementary Table S4). However, in peridotites all the spinels are altered to magnetite with total iron (i.e. Fe<sub>2</sub>O<sub>3</sub> + FeO) ranging over 69.5–86.7 wt%, low Al<sub>2</sub>O<sub>3</sub> (0.1–3.5 wt%), Cr<sub>2</sub>O<sub>3</sub> (9.7–21.2 wt%) and MgO (0.6–1.9 wt%).

#### 5.b.5. Plagioclase

Representative analyses of plagioclase from gabbros are presented in online Supplementary Table S5. The plagioclases are mostly albitized, range in composition from An<sub>65.8</sub> Ab<sub>67.9</sub> Or<sub>2.5</sub> to An<sub>31.8</sub> Ab<sub>31.7</sub> Or<sub>0.1</sub> and plot in the andesine–labradorite field in a ternary diagram (Fig. 4b) of Deer *et al.* (1992).

#### 5.b.6. Amphibole

The amphibole is absent from peridotites and pyroxenites; however, it is present in gabbros as secondary minerals, formed as a result of the break-down of pyroxenes. These amphiboles, with high Si content (5.7–7.7) and high Mg no. (61–75) (online Supplementary Table S6), show compositional variation from magnesian–hornblende to actinolite, defining a paragenetic trend as per the classification diagram of Leake (1978) (Fig. 4c).

### 5.c. Whole-rock geochemical characteristics

The peridotites, pyroxenites and gabbros from the Suru–Thasgam ophiolitic slice are characterized by a variable range of major elements with Mg no. 89–90, 76–84 (Table 1) and 56–69, respectively (Table 2). The lower concentration of alkalis (Na<sub>2</sub>O + K<sub>2</sub>O) in the pyroxenites and gabbros is explained by the cumulative nature of these rocks or is a result of alteration effects (Kakar *et al.* 2013). However, the lower LOI values of peridotites (< 4.2 wt%), pyroxenites (< 0.20 wt%) and gabbros (< 2 wt%) reflect the restricted degree of alteration.

The peridotites are characterized by a higher concentration of mantle-compatible elements, for example, Cr (2564–4025 ppm) and Ni (2565–3230 ppm), and a lower concentration of mantle-incompatible elements, for example, Nb (0.06–0.12 ppm), Zr (9–11 ppm) and Hf (0.23–0.29 ppm) in comparison to primitive mantle (PM). In addition, their higher Mg no. is similar to that of modern oceanic residual mantle peridotites (Bodinier & Godard, 2003). Similarly, the concentration of Ni, Co and Cr decreases markedly from pyroxenites (220–543 ppm for Ni, 48–151 ppm for Co and 1512–7374 ppm for Cr) to gabbros (67–189 ppm for Ni, 31–49 ppm for Co and 69–582 ppm for Cr). In Nb/Y versus SiO<sub>2</sub> classification diagram, the studied pyroxenites and gabbros show a sub-alkaline nature (online Supplementary Fig. S1a) with tholeiitic trend in the AFM ((Na<sub>2</sub>O + K<sub>2</sub>O)–Fe<sub>2</sub>O<sub>3</sub>t–MgO) plot of Irvine & Baragar (1971) (online Supplementary Fig. S1b).

The selected major- and trace-element concentrations of the studied rock types are plotted against Mg no. in online Supplementary Figure S2. These plots show distinct clusters with coherent trends from highly magnesian pyroxenites (Mg no. 76–84) to gabbroic rocks (Mg no. 56–69), perhaps reflecting magmatic differentiation. There is an observed negative correlation between CaO and Mg no. in pyroxenites and a positive correlation in gabbros reflecting plagioclase accumulation (online Supplementary Fig. S2). The high CaO/Al<sub>2</sub>O<sub>3</sub> ratios in pyroxenites (2.9–9.3; Table 1) clearly indicate the accumulation of Ca-rich clinopyroxene, whereas gabbros have a lower CaO/Al<sub>2</sub>O<sub>3</sub> ratio (0.5–1.1; Table 2), indicating accumulation of Ca-plagioclase. Cr, Ni and Co concentration decreases markedly from high values in the pyroxenites to much lower values in gabbros, consistent with fractionation of olivine, spinel and clinopyroxene. The Sr content is higher in gabbros as compared to pyroxenites, possibly because of the higher modal proportion of plagioclase in gabbros (Grove & Baker, 1984; Beard, 1986) as observed petrographically. In addition, the gabbros and pyroxenites have a lower concentration of high-field-strength elements (HFSE) such as Hf (1.5–7 and 2.4–41 ppm), Y (12–41 and 2.3–30 ppm) and Nb (0.8–5 and 0.5–56 ppm), respectively, reflecting the presence of a relatively high proportion of cumulus minerals relative to inter-cumulus liquid.

The chondrite-normalized rare earth element (REE) patterns (normalization after Sun & McDonough, 1989) for gabbros, pyroxenites and peridotites are shown in Figure 7a, b and c, respectively. The studied gabbros and pyroxenites have a higher concentration of total REE ( $\sum \text{REE} = 27.7\text{--}85.1$  and  $8.9\text{--}80.1$ , respectively) compared with peridotites (i.e.  $\sum \text{REE} = 4.35\text{--}7.1$ ). In addition, they have variable chondrite-normalized REE patterns. The gabbros contain high REE concentration compared with chondrite and display fractionated patterns (Fig. 5a) with light REE (LREE) enrichment (i.e. La<sub>N</sub>/Yb<sub>N</sub> = 2.46–5.65 and La<sub>N</sub>/Sm<sub>N</sub> = 1.07–2.28), and heavy REE (HREE) depleted patterns (i.e. Sm<sub>N</sub>/Yb<sub>N</sub> = 2.10–3.01) with negligible negative Eu anomaly. The pyroxenites contain overall enriched REE concentration compared with chondrites (Fig. 5b) and fractionated patterns with LREE enrichment (i.e. La<sub>N</sub>/Yb<sub>N</sub> = 5.65–10.98 and La<sub>N</sub>/Sm<sub>N</sub> = 3.39–4.11), slight negative Eu anomaly and flat HREE patterns (i.e. Sm<sub>N</sub>/Yb<sub>N</sub> = 1.53–2.67). The REE patterns of peridotites (Fig. 5c) show a gradual increase in REE concentrations from LREE to HREE (i.e. La<sub>N</sub>/Yb<sub>N</sub> = 0.69–1.23, La<sub>N</sub>/Sm<sub>N</sub> = 0.96–1.52 and Sm<sub>N</sub>/Yb<sub>N</sub> = 0.70–0.81).

The normal MORB basalt (N-MORB) normalized multi-element spidergram (normalization after Sun & McDonough, 1989) of gabbros is shown in Figure 6a; the primordial mantle-normalized multi-element spidergram of pyroxenites and peridotites is shown in Figure 6b and c, respectively. The studied rock types display subparallel and coherent trends in all the samples, reflecting their pristine nature. The N-MORB normalized multi-element patterns of the studied gabbros show fractionated patterns with large-ion lithophile element (LILE) enrichment (e.g. Rb, Ba, Th, U, K, Pb and Sr) and HFSE depletion (e.g. Nb, P and Ti) as compared to N-MORB (Fig. 6a). Similarly, in the primordial mantle-normalized multi-element diagram, the pyroxenites display overall enriched patterns with LILE enrichment (e.g. Rb, Ba, Th, U and Pb) and HFSE depletion (e.g. Nb, P and Ti) compared with other trace elements (Fig. 6b). In addition, the depleted Sr concentration indicates there was no plagioclase accumulation in these rock types as observed petrographically. However, the peridotites display overall depleted patterns with positive spikes of LILE (e.g. Rb, Ba, Th,

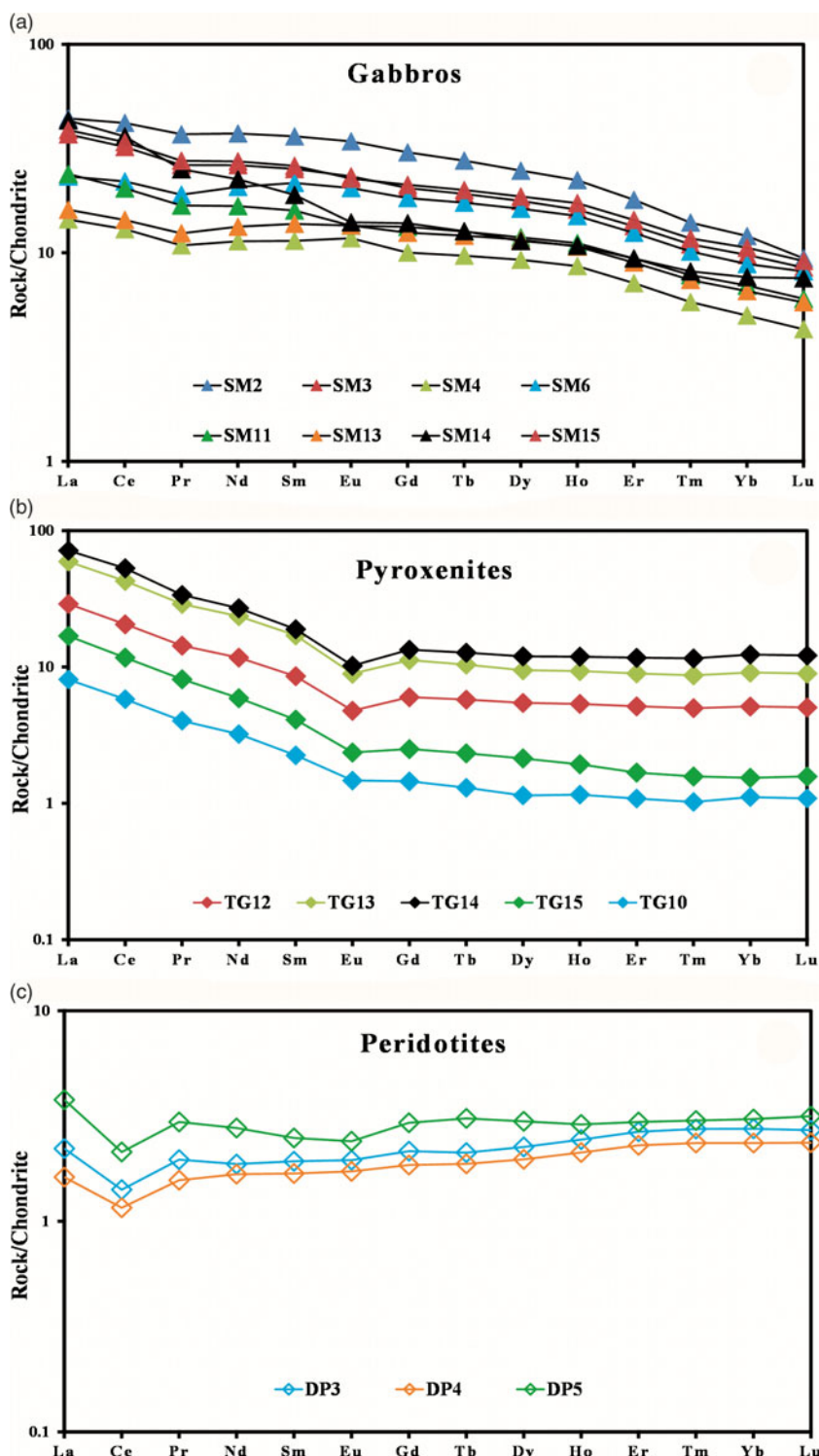


**Fig. 5.** (Colour online) Chondrite-normalized REE patterns of (a) gabbros, (b) pyroxenites and (c) peridotites from Suru-*Thasgam ophiolitic slice, western Ladakh*. Normalizing values are from Sun & McDonough (1989).

U and Pb) and a prominent negative spike of HFSE (Nb) compared with other trace elements (Fig. 6c).

## 6. Discussion

### 6.a. Post-magmatic alteration effects

The processes of metamorphism and hydrothermal alteration normally control the variable degree of elemental mobility in ophiolite

rocks (Niu, 2004). Although the studied mafic-ultramafic rock types are composed of a primary mineral assemblage of olivine, orthopyroxene, clinopyroxene, plagioclase and spinel, the petrographic observations such as the replacement of olivine with serpentine and magnetite, pyroxene with amphibole, and plagioclase with saussurite in some of the studied rock samples are consistent with metasomatic origin at lower temperatures (< 700°C; Abbott & Raymond, 1984). Further, having low LOI values (3.4–4.2 wt%) compared with highly serpentinized global peridotites, the studied

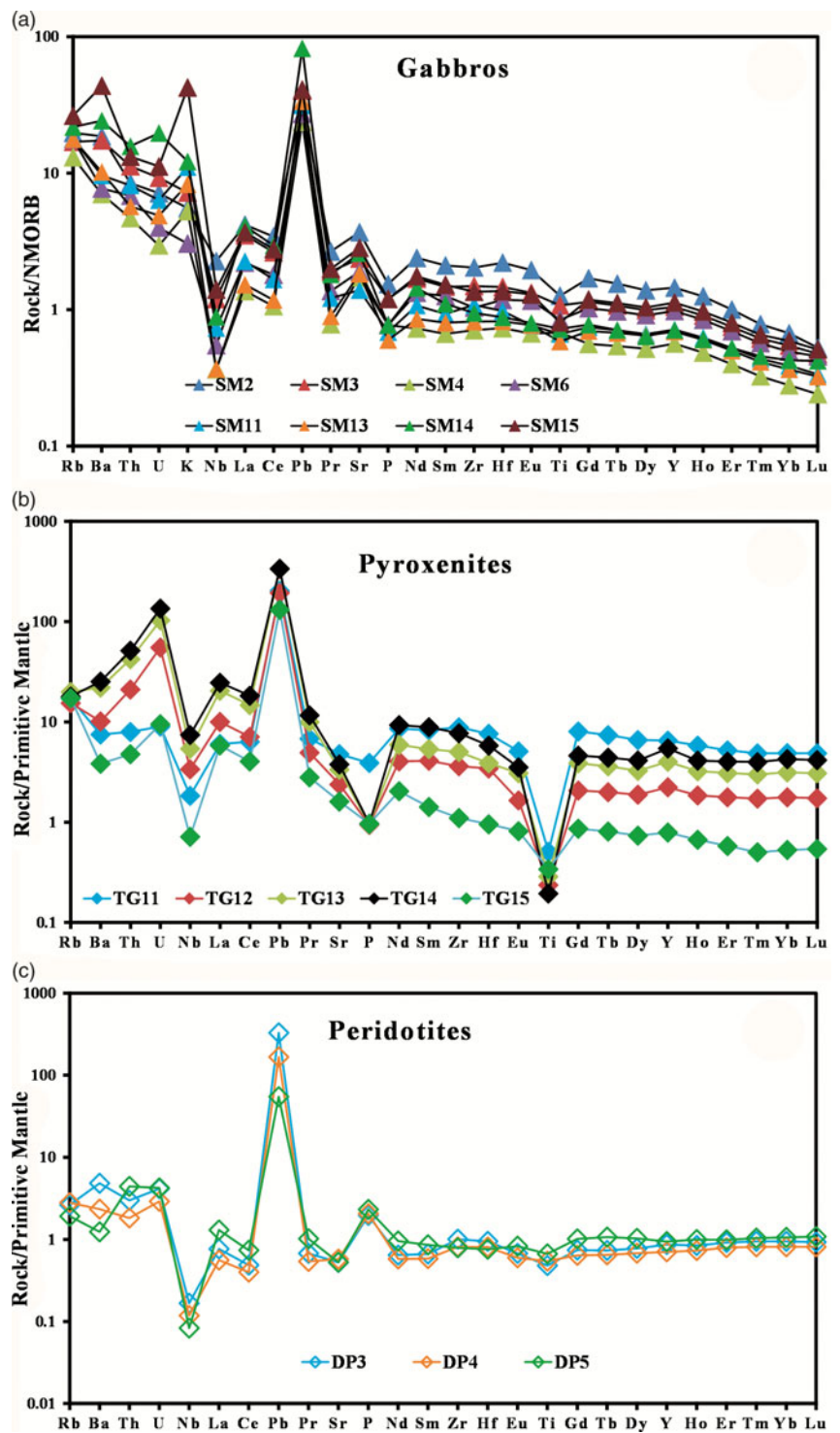


**Fig. 6.** (Colour online) (a) N-MORB-normalized spidergram of gabbros and PM-normalized spidergram of (b) pyroxenites and (c) peridotites from Suru–Thasgam ophiolitic slice, western Ladakh. Normalizing values are from Sun & McDonough (1989).

peridotites have smooth and coherent REE patterns (Fig. 5c), reflecting their least altered nature (Deschamps *et al.* 2013). Similarly, the pyroxenites and gabbros have not undergone significant secondary alteration as inferred from their low LOI values (mostly < 2 wt%), absence of Ce anomaly and lack of secondary carbonate minerals (Van Acken *et al.* 2016).

In order to evaluate the post-magmatic alteration effects in studied mafic–ultramafic rock types, we have plotted LOI values with other elements (online Supplementary Fig. S3). Elements such as Zr, Nb, La, U, Th, Pb, Rb, Ba and Sr do not show any correlation

with LOI, indicating their least mobilization. According to Polat *et al.* (2002), in mafic rocks, a  $Ce/Ce^*$  ratio (i.e. Ce anomaly) of 0.9–1.1 indicates least LREE mobility, whereas those with  $0.9 > Ce/Ce^* > 1.1$  are characterized by LREE mobility. In present study, the  $Ce/Ce^*$  ratio ranges from 1.02 to 1.1 in gabbros (except for SM10 with  $Ce/Ce^*$  ratio of 0.7) and 0.99 to 1.08 in pyroxenites, indicating limited LREE mobility. Moreover, the REE patterns of gabbros (Fig. 5a) and pyroxenites (Fig. 5b) show subparallel and coherent patterns reflecting their pristine nature. We are therefore of the opinion that the studied rock types were least

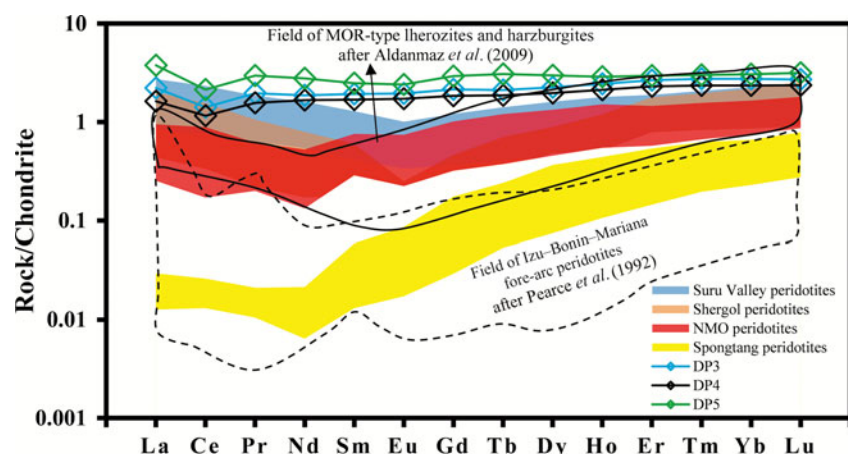


Fig. 7. (Colour online) Chondrite-normalized REE patterns of studied peridotites in comparison to other Neo-Tethyan ophiolite peridotites. Normalizing values are from Sun & McDonough (1989).

affected by the secondary processes of metamorphism and hydrothermal alteration. Major- and trace-element data describing these rock types can therefore be used to constrain their petrogenetic characteristics.

### 6.b. Nature of the protolith for peridotites

To constrain the protolith nature of the peridotites, we have focused on HFSE (e.g. Al, Ti, Nb, Hf and HREE), which are insensitive to or little affected by secondary processes (You *et al.* 1996; Bedini & Bodinier, 1999; Canil, 2004; Niu, 2004; Iyer *et al.* 2008; Deschamps *et al.* 2010, 2013). The higher whole-rock MgO, Cr, Ni and Mg no. observed in the studied peridotites with lower concentration of highly incompatible elements as compared to PM probably reflect the residual nature of their protoliths (Niu, 1997, 2004), similar to the depleted harzburgites and dunites (Zhou *et al.* 2005; Aldanmaz *et al.* 2008, 2020). However, these rocks are also characterized by Al-rich pyroxenes ( $\text{Al}_2\text{O}_3$  in orthopyroxene = 4.9–5.5 wt% and in clinopyroxene = 1.7–6.8 wt%) and Mg-rich olivines ( $\text{Fo}_{88.5-89.3}$ ), indicating that some portion of the protolith had fertile components, probably related to enrichment through slab derived fluid/melt addition (Marchesi *et al.* 2011; Parlak *et al.* 2020).

The  $\text{Al}_2\text{O}_3/\text{SiO}_2$  and  $\text{MgO}/\text{SiO}_2$  ratios of the studied peridotites range over 0.05–0.06 and 0.95–0.98, respectively (online Supplementary Fig. S4) and are similar to Shergol peridotites (0.05–0.06 and 1.09–1.2) and Suru Valley peridotites (0.04–0.06 and 0.7–0.9) (Bhat *et al.* 2019b). However, these ratios in the studied peridotites are respectively higher and lower than the highly depleted mantle residual harzburgites (i.e.  $\text{Al}_2\text{O}_3/\text{SiO}_2$  c. 0.02 and  $\text{MgO}/\text{SiO}_2$  c. 1.1; after McDonough & Sun, 1995). In Figure 7, the peridotites have HREE concentrations comparable to Neo-Tethyan MOR-type ophiolitic lherzolites and harzburgites (after Aldanmaz *et al.* 2008), Shergol and Suru Valley ophiolitic peridotites (after Bhat *et al.* 2017a, 2019b) and Nagaland-Manipur ophiolitic (NMO) tectonite peridotites (after Singh *et al.* 2017). However, these are much higher than those found in Izu-Bonin-Mariana fore-arc peridotites (after Pearce *et al.* 1992) and Spongtag ophiolitic peridotites of western Ladakh (after Maheo *et al.* 2004). Nevertheless, in a PM-normalized spidergram (Fig. 6c), the studied peridotites reflect enrichment in LILE (e.g. Rb, Ba, Th, U and Pb) and depletion in HFSE (e.g. Nb and Ti), suggesting subduction influence in their genesis (Hawkins, 2003; Niu, 2004; Bhat *et al.* 2019b).

The high Mg no. and CaO but low  $\text{TiO}_2$  content of clinopyroxenes in studied peridotites reflect derivation from depleted-mantle sources (Pearce & Norry, 1979). According to Nozaka (2010), clinopyroxenes of different origin (i.e. magmatic versus metamorphic) can be distinguished using their  $\text{Cr}_2\text{O}_3$  and  $\text{Al}_2\text{O}_3$  concentrations, as the metamorphic clinopyroxenes are extremely depleted in these elements. Clinopyroxenes in the studied peridotites have higher  $\text{Cr}_2\text{O}_3$  (mostly > 0.3 wt%) and  $\text{Al}_2\text{O}_3$  (mostly > 1 wt%) compared with those of metamorphic peridotites, confirming their igneous origin. Further, the high-magnesian olivine from the studied peridotites differs from its oceanic counterparts formed in a MOR tectonic setting that are relatively depleted in MgO (Hebert, 1982). However, studied olivine compositions show similarity to ophiolites from the SSZ, such as Kizildag (Hatay) ophiolite (Bagci *et al.* 2005), Nidar and Spongtag ophiolites (Maheo *et al.* 2004; Jonnalagadda *et al.* 2019) and Suru Valley ophiolitic slice, western Ladakh (Bhat *et al.* 2019b). Similarly, the Mg-rich orthopyroxenes in studied peridotites are reported from a number of SSZ ophiolites (DeBari & Coleman, 1989; Parlak *et al.* 1996, 2000, 2002; Bagci *et al.* 2005; Singh *et al.* 2017; Abdel Karim *et al.* 2018; Abdullah *et al.* 2018; Bhat *et al.* 2019b). From the above discussion, it therefore appears that the studied peridotites evolved in a subduction zone environment, similar to other Tethyan ophiolites such as Mirdita Ophiolite, Albania (Dilek *et al.* 2008), Albanide–Hellenide ophiolites (Saccani *et al.* 2018), Tethyan ophiolites (Dilek & Furnes 2019) and western Philippines (Yu *et al.* 2020).

### 6.c. Petrogenesis of pyroxenites and gabbros

Mantle heterogeneity could be a possibility to explain the geochemical variation observed in ophiolite rock suites (Pearce & Norry, 1979; Saccani *et al.* 2014; Saccani, 2015; Singh *et al.* 2017). The studied cumulate rock types (i.e. gabbros and pyroxenites) show subparallel and enriched chondrite-normalized REE patterns (Fig. 5), reflecting derivation from enriched mantle sources. In addition, the N-MORB-normalized spidergram of gabbros (Fig. 6a) and PM-normalized spidergram of pyroxenites (Fig. 6b) reflect selective enrichment in LILE and depletion in HFSE (e.g. Nb, P and Ti), commonly observed in subduction zone magmas (Wilson, 1989; Stern, 2004; Shervais *et al.* 2004). Such trace-element characteristics indicate melting of metasomatized mantle wedge with active participation of subducted slab component (i.e. slab fluids and/or melts) in an island-arc/SSZ tectonic setting (Wilson, 1989; Shervais *et al.*

2004). In addition, coupled enrichment of U and Th reflect the influence of subduction melts into their source regions, rather than secondary processes. Similar petrogenetic processes have been earlier explained for other mafic–ultramafic rock types along the ISZ (e.g. Maheo *et al.* 2004; Ahmad *et al.* 2008; Buckman *et al.* 2018; Bhat *et al.* 2019c) and other parts of the world (e.g. Wallin & Metcalf, 1998; Dey *et al.* 2018).

Fresh clinopyroxenes in the pyroxenites have low TiO<sub>2</sub> concentration (< 1.0% wt%) typical of non-alkaline rocks (Le Bas, 1962) and exhibit a strong affinity with intra-oceanic arc boninites similar to Egyptian ophiolites (Abd El-Rahman *et al.* 2009; Abdel Karim *et al.* 2016). Generally, SSZ ophiolitic rocks have plagioclases with higher An-content (Parlak *et al.* 2000; Bagci *et al.* 2005, 2006) such as arc-related igneous rocks (Beard, 1986; DeBarri & Coleman, 1989), Nidar ophiolites (Ahmad *et al.* 2008) and Naga Hill ophiolites, eastern India (Abdullah *et al.* 2018). The high magmatic water content and high CaO/Na<sub>2</sub>O ratio in melts are commonly assumed factors responsible for the crystallization of such calcic-plagioclases (Arculus & Wills, 1980; Panjasawatwong *et al.* 1995). However, because of hydrothermal alteration, the Ca content in plagioclases decreases and Na content increases in the studied plagioclases in gabbros, resulting in the formation of albitic plagioclases (Deer *et al.* 1992).

Further, several experimental studies have shown that the Al<sub>2</sub>O<sub>3</sub> concentration of magmatic Cr-spinel in mafic–ultramafic rocks is directly linked to the composition of parental melt (Maurel & Maurel, 1982; Kamenetsky *et al.* 2001; Rollinson, 2008) and can be calculated using the equation after Maurel & Maurel (1982), that is:

$$\text{Al}_2\text{O}_3 \text{ wt\% (spinel)} = 0.035(\text{Al}_2\text{O}_3)^{2.42} \text{ wt\% (parental melt)}.$$

This equation is based on the observation that the Al<sub>2</sub>O<sub>3</sub> concentration in spinel is a function of Al<sub>2</sub>O<sub>3</sub> concentration in melt. According to Wilson (1989), the spinel Al<sub>2</sub>O<sub>3</sub> concentration in MORB parental melt ranges from 14 to 16 wt%, whereas in boninite/arc parental melt it ranges from 10.6 to 14.4 wt%. The calculated melt composition of the studied pyroxenites have Al<sub>2</sub>O<sub>3</sub> concentration of 9–12 wt% (online Supplementary Table S4), comparable to the boninite/arc parental magma (Wilson, 1989).

The primary mineral compositions of the studied mafic–ultramafic cumulates have variable mineral compositions relative to low-pressure MORB-type parental magma (Fisk *et al.* 1980; Elthon *et al.* 1982; Parlak *et al.* 1996). The main characteristics of low pressure (c. 1 atm) crystallization phase relationships of MORB are: earlier olivine crystallization followed by plagioclase prior to pyroxene crystallization; and lower Mg no. of coexisting clinopyroxene and olivine < 82 with orthopyroxene < 74 (Elthon *et al.* 1982, 1984; Pearce *et al.* 1984). The studied mafic–ultramafic rock types contradict the low-pressure crystallization order by presence of clinopyroxene/orthopyroxene, the high Mg no. of olivine (91–88) and clinopyroxene (97–90), and the absence of plagioclase in pyroxenites (Elthon *et al.* 1982; Parlak *et al.* 1996; Singh *et al.* 2017). In Figure 8, the coexisting olivine and clinopyroxene Mg no. of pyroxenites differ from the 1-atm experiment field of MORB and overlaps with the fields of high-pressure Bay of Island ophiolite and Mersin (Turkey) ophiolite cumulates, formed at the base of island arc (Elthon *et al.* 1982; Elthon, 1991; Parlak *et al.* 1996, 2020). The presence of unzoned and compositionally constant Al- and Mg-rich clinopyroxenes, and the absence of plagioclase in studied pyroxenites, is also indicative of high-pressure (c. 10 kbar) crystallization from basaltic melts (Flower *et al.* 1977;

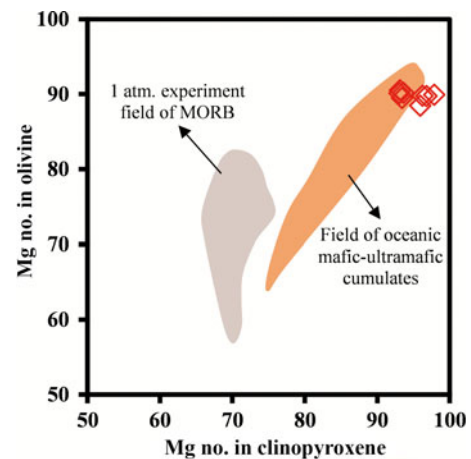


**Fig. 8.** (Colour online) Mg no. of coexisting olivine and clinopyroxene in the pyroxenites from Suru–Thasgam ophiolitic slice. Field of oceanic mafic–ultramafic cumulates represents mineral compositions of high-pressure Bay of Island ophiolite ultramafics (data after Elthon *et al.* 1982) and Mersin ophiolite ultramafics (Parlak *et al.* 1996). Grey shaded area shows experimentally determined 1-atm phase equilibria boundaries of MORB after Elthon *et al.* (1982).

Elthon *et al.* 1982; Burns, 1985; Parlak *et al.* 1996). The high-pressure crystallization phase relationship therefore seems to be consistent with the observed Suru–Thasgam ophiolitic cumulates.

#### 6.d. Tectonomagmatic implications

Various discrimination diagrams based on whole-rock trace elements or their ratios and mineral chemistry were used to put constraints on the palaeo-tectonic environment of studied rock types (Winchester & Floyd, 1977; Beccaluva *et al.* 1989; Woodhead *et al.* 1993; Stern, 2004; Condie, 2005; Wang *et al.* 2013; Nouri *et al.* 2017). In the AFM diagram of Beard (1986), the studied gabbros and pyroxenites plot in an arc-related mafic–ultramafic cumulate field (Fig. 9a). Similarly, in Th/Yb versus Nb/Yb discrimination diagram (Fig. 9b) after Pearce (2008), these rock types plot in an arc-array above the MORB–mantle array.

The orthopyroxenes in the studied peridotites are low in Al<sub>2</sub>O<sub>3</sub> < 5.45 wt% and TiO<sub>2</sub> < 0.13 wt%, but high in Mg no. (89.5–93; online Supplementary Table S2), comparable to SSZ peridotite pyroxenes (Choi *et al.* 2008; Bhat *et al.* 2019b; Jonnalagadda *et al.* 2019). Further, the presence of Mg-rich clinopyroxenes (i.e. Mg no. = 93–98 in peridotites and 90–97 in pyroxenites), Mg-rich olivines (Mg no. = 89–90 in peridotites and 89–91 in pyroxenites), and Cr-rich Al-poor spinels (Cr no. > 54 and Al no. < 29 in pyroxenites) also suggest SSZ tectonic affinity (Arai *et al.* 2006; Singh *et al.* 2017; Bhat *et al.* 2019b; Parlak *et al.* 2020).

In addition, in the Ca versus Ti diagram (Fig. 10a), the pyroxenite clinopyroxene plots in an orogenic field, indicates its sub-alkaline nature in an Al<sub>2</sub>O<sub>3</sub> versus SiO<sub>2</sub> plot (Fig. 10b), and plots in the arc-tholeiitic field in an Al versus Ti plot (Fig. 10c), similar to western Ladakh ophiolitic gabbros (Ahmad *et al.* 2008; Bhat *et al.* 2019c). Further, the studied gabbros have pargasitic composition amphiboles (Fig. 4c) correlative to island-arc affinity (Ahmad *et al.* 2008; Bhat *et al.* 2019c). These mineral characteristics are generally expected from immature island arc-affinity rocks (Stern *et al.* 2004).

Previous studies on the Dras, Suru Valley, Shergol, Spongtag and Nidar ophiolitic slices from other parts of Ladakh have shown their genetic relationship with the intra-oceanic island-arc (IOIA)

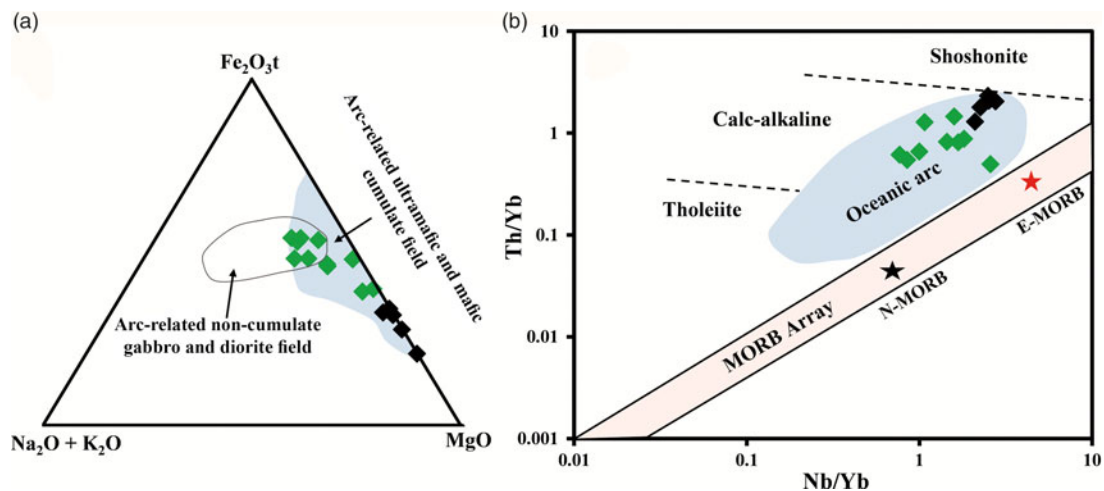


**Fig. 9.** (Colour online) Tectonomagmatic discrimination diagrams for the gabbro and pyroxenite rock types of Suru–Thasgam ophiolitic slice: (a)  $(Na_2O + K_2O) - Fe_2O_3t - MgO$  (AFM) triangular plot where fields of cumulate and non-cumulate rocks are after Beard (1986) and (b)  $Th/Yb$  versus  $Nb/Yb$  plot (after Pearce, 2008) where N-MORB – normal mid-oceanic ridge basalt; EMORB – enriched mid-oceanic ridge basalt.

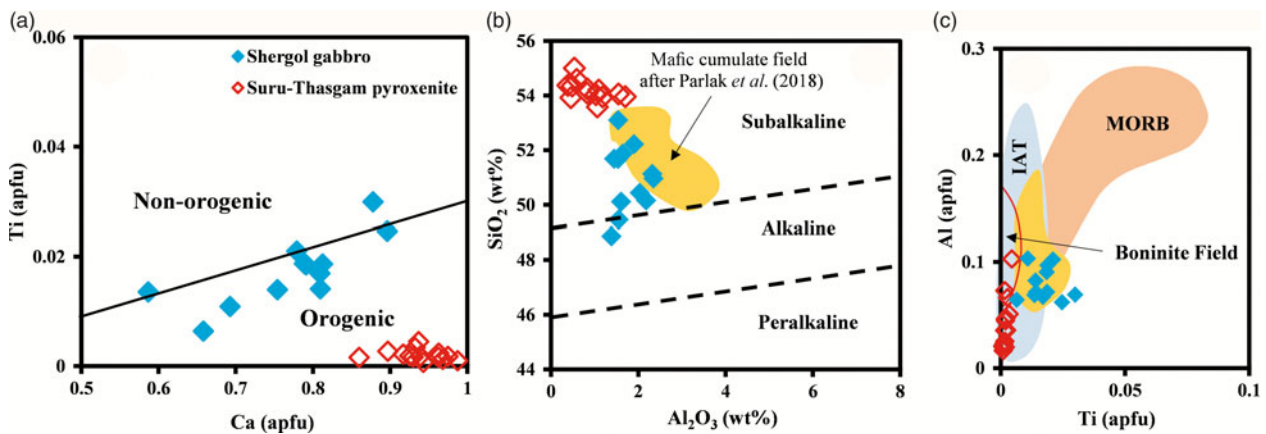


**Fig. 10.** (Colour online) Mineral discrimination diagrams of (a)  $Ca$  versus  $Ti$  after Leterrier *et al.* (1982); (b)  $Al_2O_3$  versus  $SiO_2$  after Le Bas (1962); and (c)  $Ti$  versus  $Al$  after Beccaluva *et al.* (1989) for the clinopyroxene compositions of Suru–Thasgam pyroxenites in comparison to Shergol ophiolitic gabbros, western Ladakh and mafic cumulates from Goksun Kahramanmaras ophiolite southeast Turkey after Parlak *et al.* (2020).

ophiolite complex within the Neo-Tethys Ocean (Bhat *et al.* 2020). In order to constrain the detailed geodynamic setting of the western Ladakh dismembered ophiolitic slices, we have used published age data and tectonic interpretations of these neighbouring consanguineous ophiolitic rocks. The earlier studies have reported Upper Jurassic – Middle Cretaceous ages such as zircon U–Pb ages of  $160 \pm 3$  and  $156 \pm 1$  Ma from Dras volcanics (Walsh *et al.* 2021), a U–Pb age of  $88 \pm 1$  Ma from Spong volcanics of the crustal part of Spong tang ophiolite (Pedersen *et al.* 2001), a  $^{40}Ar-^{39}Ar$  amphibole age of 130–110 Ma (Maheo *et al.* 2004) and Sm–Nd mineral–whole-rock age of  $140 \pm 32$  Ma (Ahmad *et al.* 2008) from the Nidar ophiolitic gabbros, and 136 Ma U–Pb zircon age of Spong tang ophiolite gabbros intruding the mantle peridotites (Buckman *et al.* 2018). On the basis of mineral and whole-rock geochemistry, this study suggests that the studied peridotites represent metasomatized mantle wedge peridotites in the context of the Neo-Tethys Ocean, whereas the pyroxenites and gabbros reflect high-pressure and -temperature fractionation sequences comparable to modern-day island-arc tholeiitic sequences (Fig. 11). We therefore propose that the Suru–Thasgam ophiolite

rock types represent the relict of the deeper part of the intra-oceanic Dras arc complex.

#### 6.e. Genetic relationship and modern-day analogues

The western Ladakh ophiolites of Mesozoic age have SSZ tectonic affinity preserving earlier MOR tectonic signatures (Bhat *et al.* 2019c), similar to Goksun Kahramanmaras ophiolite from SE Turkey (Parlak *et al.* 2004, 2020), Mamu Dagi ophiolite from northern Turkey (Celik *et al.* 2019) and Chaldoran ophiolite from NW Iran (Bargoshadi *et al.* 2020). In order to correlate the western Ladakh ophiolite rock types, we plotted an incompatible versus incompatible element diagram (online Supplementary Fig. S5). In Sm versus Gd (online Supplementary Fig. S5a) and Nd versus Sm (online Supplementary Fig. S5b) diagrams, the studied gabbros and pyroxenite rock types are correlative to Dras basalts and Kargil gabbros (after Bhat *et al.* 2019a), Shergol gabbros (after Bhat *et al.* 2019c), Nidar gabbros (after Ahmad *et al.* 2008) and Spong tang gabbros (after Buckman *et al.* 2018), and plot on the same differentiation line. The studied gabbro and pyroxenite rock types

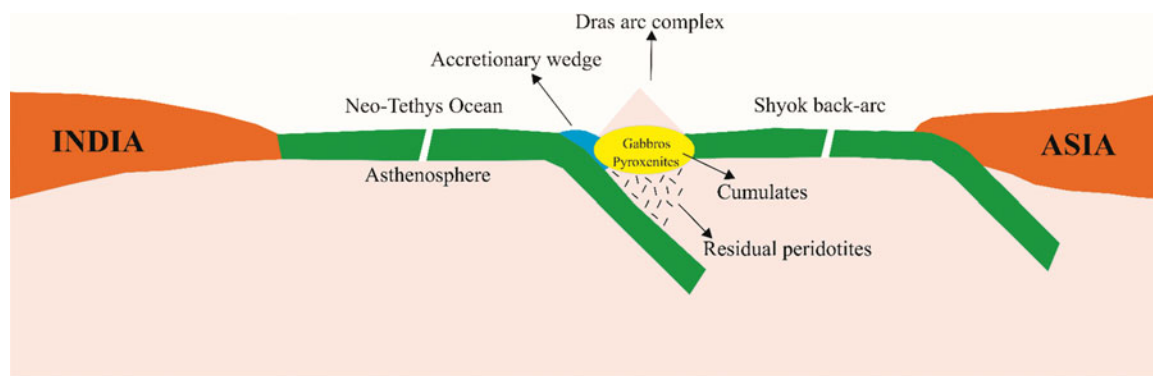


**Fig. 11.** (Colour online) Cartoon depicting proposed geodynamic model for the formation of the Suru–Thasgam ophiolitic peridotites, pyroxenites and gabbros in the context of Neo-Tethys Ocean.

therefore belong to the same SSZ tectonic setting as proposed for other ophiolitic rock types from western Ladakh (Bhat *et al.* 2019c, 2020).

Modern-day analogues of the SSZ-type ophiolites of western Ladakh are found in the Eocene Izu–Bonin–Mariana (IBM) island-arc system of the SW Pacific Ocean (Stern & Bloomer, 1992; Taylor, 1992; Ichiyama *et al.* 2020) and the Tonga arc of Papua New Guinea (Hawkins, 1995). The geochemical similarity between the IBM island-arc magmatic stratigraphy and that found in the Jurassic–Cretaceous Tethyan ophiolites suggests that the studied ophiolites were associated with the subduction initiation followed by the development of widespread island-arc complex that led to the closure of the Neo-Tethys Ocean (Reagan *et al.* 2010, 2013, 2017; Bhat *et al.* 2020).

## 7. Conclusions

This whole-rock and mineral geochemical study on peridotites, pyroxenites and gabbros from the Suru–Thasgam ophiolitic slice, western Ladakh, has led to the following conclusions.

- (1) Geochemically, the studied rock types show sub-alkaline tholeiitic characteristics and the peridotites and pyroxenites are characterized by higher Mg no. (i.e. 89–90 and 76–84, respectively) as compared to gabbros (56–69).
- (2) The peridotites show nearly flat chondrite-normalized REE patterns ( $(La/Yb)_N = 0.6–1.5$ ) while their multi-element patterns show overall depleted REE signatures with prominent Nb, a Ti negative anomaly and a Pb positive anomaly compared with PM. However, multi-element patterns of pyroxenites and gabbros show a depleted HFSE signature (e.g. Nb, P and Ti negative anomaly) and enriched LILE signature (e.g. Rb, Ba, Th, U, K, Pb and Sr positive anomaly).
- (3) The presence of Ti-poor clinopyroxenes in pyroxenites reflect their derivation from a previously depleted mantle source caused by earlier melt extraction.
- (4) The presence of highly magnesian olivine ( $Fo_{88.5–89.3}$  and  $Fo_{87.8–89.9}$ ) and clinopyroxene (Mg no. of 93–98 and 90–97, respectively) in tectonite peridotites and pyroxenites exhibits close similarity to other SSZ-related Neo-Tethyan ophiolites.
- (5) Our study suggests that the peridotites represent residual protolith nature and later evolved in a SSZ tectonic environment. However, pyroxenites and gabbros were formed by fractionation from tholeiitic melts at high pressure and temperature in an intra-oceanic island-arc tectonic setting; they are therefore

compositionally similar to those observed in modern island-arc tholeiitic sequences.

- (6) This field, mineralogical and geochemical study suggests that the Suru–Thasgam ophiolitic slice formed as part of a much larger sheet of oceanic lithosphere which accreted to the base of the intra-oceanic subduction system including Dras, Spongtag, Shergol, Suru Valley and Nidar ophiolitic slices of western Ladakh and Muslim Bagh and Bela ophiolites of Kohistan region of Pakistan. The latter were coexistent and genetically related within the same SSZ setting during the Late Cretaceous closure of the western part of the Neo-Tethys Ocean.

**Supplementary material.** To view supplementary material for this article, please visit <https://doi.org/10.1017/S0016756821000042>

**Acknowledgements.** IMB thanks the Council of Scientific and Industrial Research (CSIR), New Delhi for providing the fellowship to carry out this work. The authors are grateful to Dr AK Krishna, Dr M Satyanarayanan and Dr KSV Subramanyam from CSIR-NGRI, Hyderabad for assisting during the Laboratory work. NV Chalapathi Rao thanks DST-SERB, New Delhi, for funding the EPMA National facility at BHU, Varanasi. The authors thank the Geological Magazine Editor Dr Kathryn Goodenough and reviewers, particularly Professor Yildirim Dilek for insightful suggestions which have greatly improved the quality of the manuscript.

**Declaration of interests.** None.

## References

- Abbott RN and Raymond LA (1984) The Ashe metamorphic suite, northwest North Carolina; metamorphism and observations on geologic history. *American Journal of Science* **284**, 350–75.
- Abd El-Rahman Y, Polat A, Dilek Y, Fryer BJ, El-Sharkawy M and Sakran S (2009) Geochemistry and tectonic evolution of the Neoproterozoic incipient arc-forearc crust in the Fawakhir area, Central Eastern Desert, Egypt. *Precambrian Research* **175**, 116–34.
- Abdel-Karim AM, Ali S and El-Shafei SA (2018) Mineral chemistry and geochemistry of ophiolitic meta-ultramafics from Um Halham and Fawakhir, Central Eastern Desert, Egypt. *International Journal of Earth Sciences* **107**, 2337–55.
- Abdel-Karim AM, Ali S, Helmy HM and El-Shafei SA (2016) Fore-arc setting of the Gerf ophiolite, Eastern Desert, Egypt: evidence from mineral chemistry and geochemistry of ultramafites. *Lithos* **263**, 52–65.
- Abdullah S, Misra S and Ghosh B (2018) Melt-rock interaction and fractional crystallization in the Moho transition Zone: evidence from the cretaceous Naga Hills Ophiolite, North-East India. *Lithos* **322**(1), 197–211, <https://doi.org/10.1016/j.lithos.2018.10.012>.



- Ahmad T, Islam R, Khanna PP and Thakur VC** (1996) Geochemistry, petrogenesis and tectonic significance of the basic volcanic units of the Zildat ophiolitic mélange, Indus suture zone, eastern Ladakh (India). *Geodinamica Acta* **9**, 222–33.
- Ahmad T, Tanaka T, Sachan HK, Asahara Y, Islam R and Khanna PP** (2008) Geochemical and isotopic constraints on the age and origin of the Nidar Ophiolitic Complex, Ladakh, India: implications for the Neo-Tethyan subduction along the Indus suture zone. *Tectonophysics* **451**, 206–24.
- Aitchison JC, Baxter AT, Zyabrev SV and Ali JR** (2011) Upper Jurassic radiolarians from the Naga Ophiolite, Nagaland, Northeast India. *Gondwana Research* **20**, 638–44.
- Aldanmaz E, Schmidt MW, Gourgaud A and Meisel T** (2009) Mid-ocean ridge and supra-subduction geochemical signatures in spinel–peridotites from the Neotethyan ophiolites in SW Turkey: implications for upper mantle melting processes. *Lithos* **113**(3–4), 691–708.
- Aldanmaz E, van Hinsbergen DJ, Yildiz-Yuksekol O, Schmidt MW, McPhee PJ, Meisel T, Guctekin A and Mason PR** (2020) Effects of reactive dissolution of orthopyroxene in producing incompatible element depleted melts and refractory mantle residues during early fore-arc spreading: constraints from ophiolites in eastern Mediterranean. *Lithos* **360**, 105438.
- Aldanmaz E, Yaliniz MK, Guctekin A and Goncuoglu MC** (2008) Geochemical characteristics of mafic lavas from the Neotethyan ophiolites in western Turkey: implications for heterogeneous source contribution during variable stages of ocean crust generation. *Geological Magazine* **145**, 37–54.
- Arai S, Kadoshima K and Morishita T** (2006) Widespread arc-related melting in the mantle section of the northern Oman ophiolite as inferred from detrital chromian magnesio chromites. *Journal of the Geological Society of London* **163**, 869–79.
- Arculus RJ and Wills KJA** (1980) The petrology of plutonic blocks and inclusions from Lesser Antilles island arc. *Journal of Petrology* **21**, 743–99.
- Bagci U, Parlak O and Hock V** (2005) Whole rock and mineral chemistry of cumulates from the Kizildag (Hatay) ophiolite (Turkey): clues for multiple magma generation during crustal accretion in the southern Neotethyan Ocean. *Mineralogical Magazine* **69**, 39–62.
- Bagci U, Parlak O and Hock V** (2006) Geochemical character and tectonic environment of ultramafic to mafic cumulates from the Tekirova (Antalya) ophiolite (southern Turkey). *Geological Journal* **41**, 193–219.
- Bargoshadi RM, Moazzen M and Yang TN** (2020) Geochemistry of arc-related mantle peridotites and gabbros from the Chaldoran ophiolite, NW Iran. *International Geology Review* **62**, 1724–50.
- Beard JS** (1986) Characteristic mineralogy of arc-related cumulate gabbros: implications for the tectonic setting of gabbroic plutons and for andesite genesis. *Geology* **14**, 848–51.
- Beccaluva L, Macciotta G, Piccardo GB and Zeda O** (1989) Clinopyroxene composition of ophiolite basalts as petrogenetic indicator. *Chemical Geology* **77**, 165–82.
- Bedini RM and Bodinier JL** (1999) Distribution of incompatible trace elements between the constituents of spinel peridotite xenoliths: ICP-MS data from the East African Rift. *Geochimica et Cosmochimica Acta* **63**(22), 3883–900.
- Bhat IM, Ahmad T and Subba Rao DV** (2017a) Geochemical characterization of serpentinized peridotites from the Shergol ophiolitic slice along the Indus Suture Zone (ISZ), Ladakh Himalaya, India. *The Journal of Geology* **125**, 501–13.
- Bhat IM, Ahmad T and Subba Rao DV** (2017b) Compositional variability of spinel–group minerals from the Shergol serpentinized peridotites along Indus suture zone, Ladakh Himalaya (India): constraints on tectono-magmatic history. *Chemie der Erde Geochemistry* **77**, 587–95.
- Bhat IM, Ahmad T and Subba Rao DV** (2019a) The tectonic evolution of Dras arc complex along Indus Suture Zone, western Himalaya: implications for Neo-Tethys geodynamics. *Journal of Geodynamics* **124**, 52–66.
- Bhat IM, Ahmad T and Subba Rao DV** (2019b) Origin and evolution of Suru Valley ophiolite peridotite slice along Indus suture zone, Ladakh Himalaya, India: implications on melt–rock interaction in a subduction zone environment. *Chemie der Erde Geochemistry* **79**, 78–93.
- Bhat IM, Ahmad T and Subba Rao DV** (2019c) Petrology and geochemistry of mafic intrusive rocks from the Sapi–Shergol ophiolitic mélange, Indus Suture Zone, western Ladakh: constraints on petrogenesis and tectonic setting. *The Journal of Geology* **127**, 543–66.
- Bhat IM, Ahmad T, Subba Rao DV, Balakrishnan S and Chalapathi Rao NV** (2021) PGE and isotopic constraints on Shergol and Suru Valley Ophiolites: implication for petrogenesis and supra-subduction tectonics in ISZ, Ladakh Himalaya. *Geoscience Frontiers* **12**(3), 101118, <https://doi.org/10.1016/j.gsf.2020.11.014>.
- Bodinier JL and Godard M** (2003) Orogenic, ophiolitic and abyssal peridotites. In *The Mantle and Core* (ed. RW Carlson). pp. 103–170. Amsterdam: Elsevier, 2.
- Brookfield ME and Reynolds PH** (1981) Late Cretaceous emplacement of the Indus suture zone ophiolitic mélanges and an Eocene–Oligocene magmatic arc on the northern edge of the Indian plate. *Earth and Planetary Science Letters* **55**, 157–162.
- Buckman S, Aitchison JC, Nutman A, Bennett V, Saktura WM, Walsh J, Kachovich S and Hidaka H** (2018) The Spongtang Massif in Ladakh, NW Himalaya: an Early Cretaceous record of spontaneous, intra-oceanic subduction initiation in the Neotethys. *Gondwana Research* **63**, 226–49.
- Burns LE** (1985) The Border Ranges ultramafic and mafic complex, south central Alaska: cumulate fractionates of island arc volcanics. *Canadian Journal of Earth Sciences* **22**, 1020–38.
- Canil D** (2004) Mildly incompatible elements in peridotites and the origins of mantle lithosphere. *Lithos* **77**, 375–93.
- Celik OF, Topuz G, Billor Z and Ozkan M** (2019) Middle Jurassic subduction-related ophiolite fragment in Triassic accretionary complex (Mamu Dagi ophiolite, Northern Turkey). *International Geology Review* **61**, 2021–35.
- Choi SH, Shervais JW and Mukasa SB** (2008) Supra-subduction and abyssal mantle peridotites of the coast range ophiolite, California. *Contributions to Mineralogy and Petrology* **156**, 551–76.
- Coleman RG** (1977) *Ophiolites—Ancient Continental Lithosphere*. New York, Berlin: Springer Verlag, 220 pp.
- Condie K** (2005) High field strength element ratios in Archean basalts: a window to evolving sources of mantle plumes. *Lithos* **79**, 491–504.
- DeBari SM and Coleman RG** (1989) Examination of the deep levels of an island arc: evidence from the Tonsina ultramafic–mafic assemblage, Tonsina, Alaska. *Journal of Geophysical Research* **94**, 4373–91.
- Deer WA, Howie RA and Zussman J** (1992) *An Introduction to the Rock-forming Minerals*, second edition. London: Pearson Prentice Hall, 696 pp.
- Deschamps F, Godard M, Guillot S and Hattori K** (2013) Geochemistry of subduction zone serpentinites: a review. *Lithos* **178**, 96–127.
- Deschamps F, Guillot S, Godard M, Chauvel C, Andreani M and Hattori K** (2010) In situ characterization of serpentinites from forearc mantle wedges: timing of serpentinization and behavior of fluid–mobile elements in subduction zones. *Chemical Geology* **269**, 262–77.
- Dey A, Hussain MF and Barman MN** (2018) Geochemical characteristics of mafic and ultramafic rocks from the Naga Hills Ophiolite, India: implications for petrogenesis. *Geoscience Frontiers* **9**, 517–29.
- Dilek Y and Furnes H** (2009) Structure and geochemistry of Tethyan ophiolites and their petrogenesis in subduction rollback systems. *Lithos* **113**, 1–20.
- Dilek Y and Furnes H** (2011) Ophiolite genesis and global tectonics: geochemical and tectonic fingerprinting of ancient oceanic lithosphere. *Bulletin of the Geological Society of America* **123**, 387–411.
- Dilek Y and Furnes H** (2014) Ophiolites and their origins. *Elements* **10**, 93–100.
- Dilek Y and Furnes H** (2019) Tethyan ophiolites and Tethyan seaways. *Journal of the Geological Society of London* **176**, 899–912.
- Dilek Y, Furnes H and Shallo M** (2008) Geochemistry of the Jurassic Mirdita Ophiolite (Albania) and the MORB to SSZ evolution of a marginal basin oceanic crust. *Lithos* **100**, 174–209.
- Dilek Y and Newcomb S** (2003) Ophiolite concept and the evolution of the geological thought. *Geological Society of America Special Paper* **373**, 1–16.
- Dilek Y and Robinson PT** (2003) Ophiolites in earth history. *Geological Society of London Special Publications* **218**, 1–8.
- Elthon D** (1991) Geochemical evidence for formation of the Bay of Island ophiolite above subduction zone. *Nature* **354**, 140–3.
- Elthon D, Casey JF and Komor S** (1982) Mineral chemistry of ultramafic cumulates from the North Arm Mountain Massif of the Bay of Islands ophiolite: evidence for high-pressure crystal fractionation of oceanic basalts. *Journal of Geophysical Research* **87**, 8717–8734.

- Elthon D, Casey JF and Komor S** (1984) Cryptic mineral chemistry variations in a detailed traverse through the cumulate ultramafic rocks of the North Arm Mountain massif of the Bay of Island ophiolite, Newfoundland. In *Ophiolites and Oceanic Lithosphere* (ed. IG Gass, SJ Lippard and AW Shelton), pp. 83–97. London: Blackwell.
- Fisk MR, Schilling JG and Sigurdsoon H** (1980) An experimental investigation of Iceland and Reykjanes Ridge tholeiites. I. Phase relations. *Contributions to Mineralogy and Petrology* **74**, 361–74.
- Flower MFJ, Robinson PT, Schmincke HU and Ohnmacht W** (1977) Magma fractionation systems beneath the Mid-Atlantic ridge at 36–37°N. *Contributions to Mineralogy and Petrology* **64**, 167–95.
- Furnes H, Dilek Y, Zhao G, Safonova I and Santosh M** (2020) Geochemical characterization of ophiolites in the Alpine-Himalayan Orogenic Belt: magmatically and tectonically diverse evolution of the Mesozoic Neotethyan oceanic crust. *Earth-Science Reviews* **208**, 103258.
- Grove TL and Baker MB** (1984) Phase equilibrium controls on the tholeiitic versus calc-alkaline differentiation trends. *Journal of Geophysical Research* **89**, 3253–74.
- Hawkins JW** (1995) Evolution of the Lau basin: insights from ODP Leg 135. In *Active Margins and Marginal Basins of the Western Pacific* (ed. B Taylor and J Natland), 88, pp. 125–173. Washington, DC: American Geophysical Union.
- Hawkins JW** (2003) Geology of supra-subduction zones-implications for the origin of ophiolites. *Geological Society of America Special Paper* **373**, 227–68.
- Hebert R** (1982) Petrography and mineralogy of oceanic peridotites and gabbros: some comparisons with ophiolite examples. *Ophioliti* **2**, 299–324.
- Hebert R, Bezard R, Guilmette C, Dostal J, Wang CS and Liu ZF** (2012) The Indus-Yarlung Zangbo ophiolites from Nanga Parbat to Namche Barwa syntaxes, southern Tibet: first synthesis of petrology, geochemistry, and geochronology with incidences on geodynamic reconstructions of Neo-Tethys. *Gondwana Research* **22**, 377–97.
- Hodel F, Triantafyllou A, Berger J, Macouin M, Baele JM, Mattioli N, Monnier C, Trindade RIF, Ducea MN, Chatir A and Ennih N** (2020) The Moroccan Anti-Atlas ophiolites: timing and melting processes in an intra-oceanic arc-back-arc environment. *Gondwana Research* **86**, 182–202.
- Honegger K, Dietrich V, Frank W, Gansser A, Thoni M and Trommsdorf V** (1982) Magmatic and metamorphism in the Ladakh Himalayas (the Indus-Tsangpo suture zone). *Earth and Planetary Science Letters* **60**, 253–92.
- Ichihaya Y, Koshiba T, Ito H and Tamura A** (2020) Geochemistry and magmatic zircon U–Pb dating of amphibolite blocks in the Omi serpentinite mélange, north central Japan: possible subduction of the Cambrian oceanic crust. *Journal of Mineralogical and Petrological Sciences* **115**(4), 313–21, 191205.
- Irvine TN and Baragar WRA** (1971) A guide to the chemical classification of the common volcanic rocks. *Canadian Journal of Earth Science* **8**, 523–48.
- Iyer K, Austrheim H, John T and Jamtveit B** (2008) Serpentinization of the oceanic lithosphere and some geochemical consequences: constraints from the Leka Ophiolite Complex, Norway. *Chemical Geology* **249**, 66–90.
- Jadoon UK, Ding L, Baral U and Qasim M** (2020) Early Cretaceous to Eocene magmatic records in Ladakh arc: Constraints from U–Pb ages of Deosai volcanics, northern Pakistan. *Geological Journal* **55**(7), 5384–97, <https://doi.org/10.1002/gj.3730>.
- Jonnalagadda MK, Karmalkar NR, Benoit M, Gregoire M, Duraiswami RA, Harshe S and Kamble S** (2019) Compositional variations of chromian spinels from peridotites of the Spontang ophiolite complex, Ladakh, NW Himalayas, India: petrogenetic implications. *Geosciences Journal* **6**, 895–915.
- Kakar IM, Khalid M, Khan M, Kasi AK and Manan RA** (2013) Petrology and geochemistry of gabbros from the Muslim Bagh Ophiolite: implications for their petrogenesis and tectonic setting. *Journal of Himalayan Earth Sciences* **46**, 19–30.
- Kamenetsky VS, Crawford AJ and Meffre S** (2001) Factors controlling chemistry of magmatic spinel: an empirical study of associated olivine, Cr-spinel and melt inclusions from primitive rocks. *Journal of Petrology* **42**, 655–71.
- Kingson O, Bhutani R, Dash JK, Sebastian S and Balakrishnan S** (2017) Resolving the conundrum in origin of the Manipur Ophiolite Complex, Indo-Myanmar range: constraints from Nd isotopic ratios and elemental concentrations in serpentinized peridotite. *Chemical Geology* **460**, 117–29.
- Krishna AK, Murthy NN and Govil PK** (2007) Multi-element analysis of soils by wavelength-dispersive X-ray fluorescence spectrometry. *Atomic Spectroscopy* **28**, 202–14.
- Le Bas NJ** (1962) The role of aluminum in igneous clinopyroxenes with relation to their parentage. *American Journal of Science* **260**, 267–88.
- Leake BE** (1978) Nomenclature of amphiboles. *Canadian Mineralogist* **16**, 501–20.
- Letierrier J, Maury RC, Thonon P, Girard D and Marechal M** (1982) Clinopyroxene composition as a method of identification of the magmatic affinities of paleovolcanic series. *Earth and Planetary Science Letters* **59**, 139–54.
- Liu CZ, Zhang C, Xu Y, Wang JG, Chen Y, Guo S, Wu FY and Sein K** (2016) Petrology and geochemistry of mantle peridotites from the Kalaymyo and Myitkyina ophiolites (Myanmar): implications for tectonic settings. *Lithos* **264**, 495–508.
- Maheo G, Bertrand H, Guillot S, Villa IM, Keller F and Capiez P** (2004) The south Ladakh ophiolites (NW Himalaya, India): an intraoceanic tholeiitic origin with implication for the closure of the Neo-Tethys. *Chemical Geology* **203**, 273–303.
- Maheo G, Fayoux X, Guillot S, Garzanti E, Capiez P and Mascle G** (2006) Relicts of an intra-oceanic arc in the Sapi-Shergol melange zone (Ladakh, NW, Himalaya, India): implications for the closure of the Neo-Tethys Ocean. *Journal of Asian Earth Sciences* **26**, 695–707.
- Marchesi C, Jolly WT, Lewis JF, Garrido CJ, Proenza JA and Lidiak EG** (2011) Petrogenesis of fertile mantle peridotites from the Monte del Estado massif (Southwest Puerto Rico): a preserved section of Proto-Caribbean lithospheric mantle? *Geologica Acta* **9**, 289–306.
- Maurel C and Maurel P** (1982) Etude expérimentale de la distribution de l'aluminium entre bain silicate basique et spinelle chromifère. Implications pétrogénétiques: teneur en chrome des spinelles. *Bulletin de Mineralogy* **105**, 197–202.
- McDonough WF and Sun SS** (1995). The composition of the Earth. *Chemical Geology* **120**, 223–53.
- Moore EM, Kellogg L and Dilek Y** (2000) Tethyan ophiolites, mantle convection, and tectonic historical contingency: a resolution of the ophiolite conundrum. *Geological Society of America Special Paper* **349**, 3–12.
- Morimoto N, Fabries J, Ferguson AK, Ginzburg IV, Ross M, Seifert FA and Zussman J** (1989) Nomenclature of pyroxenes. *Canadian Mineralogist* **27**, 143–56.
- Niu Y** (1997) Mantle melting and melt extraction processes beneath ocean ridges: evidence from abyssal peridotites. *Journal of Petrology* **38**, 1047–74.
- Niu Y** (2004) Bulk-rock major and trace element compositions of abyssal peridotites: implications for mantle melting, melt extraction and post-melting processes beneath mid-ocean ridges. *Journal of Petrology* **45**, 2423–58.
- Nouri F, Ashara Y, Azizi H and Yamamoto K** (2017) Geochemistry and petrogenesis of the Eocene back arc mafic rocks in the Zagros suture zone, northern Noorabad, western Iran. *Chemie der Erde, Geochemistry* **77**, 517–533.
- Nozaka T** (2010) A note on compositional variation of olivine and pyroxene in thermally metamorphosed ultramafic complexes from SW Japan. *Okayama University Earth Science Reports* **17**, 1–5.
- Panasawatwong Y, Danyushevsky LV, Crawford AJ and Harris KL** (1995) An experimental study of the effects of melt composition on plagioclase-melt equilibria at 5 and 10 kbars: implications for the origin of magmatic high-An plagioclase. *Contributions to Mineralogy and Petrology* **118**, 420–32.
- Parlak O, Bagci U, Rizaoglu T, Ionescu C, Onal G, Hock V and Kozlu H** (2020) Petrology of ultramafic to mafic cumulate rocks from the Goksun (Kahramanmaraş) ophiolite, southeast Turkey. *Geoscience Frontiers* **11**, 109–28.
- Parlak O, Delaloye M and Bingol E** (1996) Mineral chemistry of ultramafic and mafic cumulates as an indicator of the arc-related origin of the Mersin ophiolite (southern Turkey). *Geologische Rundschau* **85**, 647–61.
- Parlak O, Hock V and Delaloye M** (2000) Supra-subduction zone origin of the Pozanti-Karsanti ophiolite (southern Turkey) deduced from whole-rock and mineral chemistry of the gabbroic cumulates. In *Tectonics and Magmatism in Turkey and the Surrounding Area* (eds E Bozkurt, JA Winchester and JDA Piper), pp. 219–34. Geological Society of London, Special Publication no. 173.

- Parlak O, Hock V and Delaloye M** (2002) The supra-subduction zone Pozanti-Karsanti ophiolite, southern Turkey: evidence for high-pressure crystal fractionation of ultramafic cumulates. *Lithos* **65**, 205–24.
- Parlak O, Hock V, Kozlu H and Delaloye M** (2004) Oceanic crust generation in an island arc tectonic setting, SE Anatolian Orogenic Belt (Turkey). *Geological Magazine* **141**, 583–603.
- Pearce JA** (2008) Geochemical fingerprinting of oceanic basalts with applications to ophiolite classification and the search for Archean oceanic crust. *Lithos* **100**, 14–48.
- Pearce JA** (2014) Immobile element fingerprinting of ophiolites. *Elements* **10**, 101–8.
- Pearce JA, Lippard SJ and Roberts S** (1984) Characteristics and tectonic significance of supra-subduction ophiolites. In *Marginal Basin Geology: Volcanic and Associated Sedimentary and Tectonic Processes in Modern and Ancient Marginal Basins* (eds BP Kokelaar and MF Howells), pp. 777–94. Geological Society of London, Special Publication no. 16.
- Pearce JA and Norry ML** (1979) Petrogenetic implications of Ti, Zr, Y and Nb variations in volcanic rocks. *Contributions to Mineralogy and Petrology* **69**, 33–47.
- Pearce JA, van der Laan SR, Arculus RJ, Murton BJ, Ishii T, Peate DW and Parkinson IJ** (1992) Boninite and harzburgite from Leg 125 (Bonin-Mariana forearc): a case study of magma genesis during the initial stages of subduction. In *Proceedings of the Ocean Drilling Program, Scientific Results* (eds P Fryer, JA Pearce and LB Stokking, et al.), 125, pp. 623–659. College Station, TX: Texas A&M University.
- Pedersen RB, Searle MP and Corfield RI** (2001) U–Pb zircon ages from the Spontang Ophiolite, Ladakh Himalaya. *Journal of the Geological Society of London* **158**, 513–20.
- Polat A, Hofman, AW and Rosing M** (2002) Boninite-like volcanic rocks in the 3.7–3.8 Ga Isua greenstone belt West Greenland: geochemical evidence for intra-oceanic subduction zone processes in the early Earth. *Chemical Geology* **184**, 231–54.
- Radhakrishna T, Divakara Rao V and Murali AV** (1984) Geochemistry of Dras volcanics and the evolution of the Indus suture ophiolites. *Tectonophysics* **108**, 135–53.
- Radhakrishna T, Divakara Rao V and Murali AV** (1987) Geochemistry and petrogenesis of ultramafic and mafic plutonic rocks of the Dras ophiolitic mélange, Indus suture (northwest Himalaya). *Earth and Planetary Science Letters* **82**, 136–44.
- Reagan MK, Ishizuka O, Stern RJ, Kelley KA, Ohara Y, Blichert-Toft J, Bloomer SH, Cash J, Fryer P, Hanan B, Hickey-Vargas R, Ishii T, Kimura JI, Peate DW, Rowe MC and Woods M** (2010) Fore-arc basalts and subduction initiation in the Izu-Bonin-Mariana system. *Geochemistry Geophysics Geosystems* **11**, 1–17.
- Reagan MK, McClelland WC, Girard G, Goff KR, Peate DW, Ohara Y and Stern RJ** (2013) The geology of the southern Mariana fore-arc crust: implications for the scale of Eocene volcanism in the western Pacific. *Earth and Planetary Science Letters* **380**, 41–51.
- Reagan MK, Pearce JA, Petronotis K, Almeev RR, Avery AJ, Carvalho C, Chapman T, Christeson GL, Ferre EC, Godard M, Heaton DE, Kirchenbaur M, Kurz W, Kutterolf S, Li H, Li Y, Michibayashi K, Morgan S, Nelson WR, Prytulak J, Python M, Robertson AHF, Ryan JG, Sager WW, Sakuyama T, Shervais JW, Shimizu K and Whattam SA** (2017) Subduction initiation and ophiolite crust: new insights from IODP drilling. *International Geology Review* **59**, 1439–50.
- Reuber I** (1989) The Dras Arc - two successive volcanic events on eroded oceanic-crust. *Tectonophysics* **161**, 93–106.
- Reuber I, Montigny R, Thuizat R and Heitz A** (1990) K/Ar ages of ophiolites and arc volcanics of the Indus suture zone (Ladakh): comparison with other Himalaya–Karakorum data. *Journal of Himalayan Geology* **1**, 115–25.
- Robertson AHF** (2000) Formation of melanges in the Indus Suture Zone, Ladakh Himalaya by successive subduction-related, collisional and post-collisional processes during late Mesozoic late tertiary time. In *Tectonics of the Nanga Parbat Syntaxis and the Western Himalaya* (eds MA Khan, PJ Treolar, MP Searle and MQ Jan), pp. 333–74. Geological Society of London, Special Publication no. 170.
- Robertson A and Degnan P** (1994) The Dras arc complex - lithofacies and reconstruction of a Late Cretaceous oceanic volcanic arc in the Indus suture zone, Ladakh-Himalaya. *Sedimentary Geology* **92**, 117–45.
- Rollinson H** (2008) The geochemistry of mantle chromitites from the northern part of the Oman ophiolite: inferred parental melt compositions. *Contributions to Mineralogy and Petrology* **156**, 273–88.
- Saccani E** (2015) A new method of discriminating different types of post-Archean ophiolitic basalts and their tectonic significance using Th-Nb and Ce-Dy-Yb systematics. *Geoscience Frontiers* **6**, 481–501.
- Saccani E, Allahyari K and Rahimzadeh B** (2014) Petrology and geochemistry of mafic magmatic rocks from the Sarve-Abad ophiolites (Kurdistan region, Iran): evidence for interaction between MORB-type asthenosphere and OIB-type components in the southern Neo-Tethys Ocean. *Tectonophysics* **621**, 132–47.
- Saccani E, Dilek Y and Photiades A** (2018) Time-progressive mantle-melt evolution and magma production in a Tethyan marginal sea: a case study of the Albanide–Hellenide ophiolites. *Lithosphere* **10**, 35–53.
- Satyannarayanan M, Balaram V, Sawant SS, Subramanyam KSV and Krishna GV** (2014) High-precision multi-element analysis on geological samples by HR-ICP-MS. In *Proceedings of 28<sup>th</sup> Indian Society for Mass Spectrometry Symposium cum Workshop on Mass Spectrometry*, Parwanoo, pp. 181–184. Mumbai: Indian Society for Mass Spectrometry.
- Shervais JW, Kimbrough DL, Renne P, Hanan BB, Murchey B, Snow CA, Zoglman Schuman MM and Beaman J** (2004) Multi-stage origin of the Coast Range ophiolite, California: implications for the life cycle of supra-subduction zone ophiolites. *International Geology Review* **46**, 289–315.
- Singh AK, Nayak R, Khogenkumar S, Subramanyam KSV, Thakur SS, Bikramaditya Singh RK and Satyanarayanan M** (2017) Genesis and tectonic implications of cumulate pyroxenites and tectonite peridotites from the Nagaland–Manipur ophiolites, Northeast India: constraints from mineralogical and geochemical characteristics. *Geological Journal* **52**, 415–36.
- Stern RJ** (2004) Subduction initiation: spontaneous and induced. *Earth and Planetary Science Letters* **226**, 275–92.
- Stern RJ and Bloomer SH** (1992) Subduction zone infancy: examples from the Eocene Izu-Bonin-Mariana and Jurassic California arcs. *Bulletin of Geological Society of America* **104**, 1621–36.
- Stern RJ, Johnson PR, Kroner A and Yibas B** (2004) Neoproterozoic ophiolites of the Arabian-Nubian Shield. In *Precambrian Ophiolites and Related Rocks* (ed. T Kusky), pp. 95–128. Amsterdam: Elsevier, Developments in Precambrian Geology, no. 13.
- Sun SS and McDonough WF** (1989) Chemical and isotopic systematics of oceanic basalts: implications for mantle composition and processes. In *Magmatism in the Ocean Basins* (eds AD Saunders and MJ Norry), pp. 313–45. Geological Society of London, Special Publication no. 42.
- Taylor B** (1992) Rifting and the volcanic-tectonic evolution of the Izu-Bonin Mariana arc. In *Proceedings of the Ocean Drilling Program, Scientific Results* (ed. B Taylor and K Fujioka), pp. 627–651. College Station, TX: Texas A&M University.
- Van Acken D, Hoffmann JE, Schorscher JHD, Schulz T, Heuser A and Luguët A** (2016) Formation of high-Al komatiites from the Mesoarchean Quebra Osso Group, Minas Gerais, Brazil: trace elements, HSE systematics and Os isotopic signatures. *Chemical Geology* **422**, 108–21.
- Wallin ET and Metcalf V** (1998) Supra-subduction zone ophiolites formed in an extensional forearc: Trinity Terrae, Kalmath Mountains, California. *The Journal of Geology* **106**, 591–608.
- Walsh JMJ, Buckman S, Nutman AP and Zhou R** (2021) The significance of Upper Jurassic felsic volcanic rocks within the incipient, intraoceanic Dras Arc, Ladakh, NW Himalaya. *Gondwana Research* **90**, 199–219.
- Wang Y, Zhang A, Fan W and Zhang Y** (2013) Origin of paleo subduction modified mantle for Silurian gabbro in the Cathaysia Block: geochronological and geochemical evidence. *Lithos* **160**, 37–54.
- Wilson M** (1989) *Igneous Petrogenesis, a Global Tectonic Approach*. London: Chapman and Hall, 470 pp.
- Winchester JA and Floyd PA** (1977) Geochemical discrimination of different magma series and their differentiation products using immobile elements. *Chemical Geology* **20**, 325–43.

- Woodhead J, Eggins S and Gamble J** (1993) High field strength and transition element systematics in island arc and back-arc basin basalts: evidence for multi-phase melt extraction and a depleted mantle wedge. *Earth and Planetary Science Letters* **114**, 491–504.
- Xiong F, Yang J, Robinson PT, Gao J, Chen Y and Lai S** (2017) Petrology and geochemistry of peridotites and podiform chromitite in the Xigaze ophiolite, Tibet: implications for a supra-subduction zone origin. *Journal of Asian Earth Sciences* **146**, 56–75.
- You CF, Castillo PR, Gieskes JM, Chan LH and Spivack AJ** (1996) Trace element behavior in hydrothermal experiments: implications for fluid processes at shallow depths in subduction zones. *Earth and Planetary Science Letters* **140**, 41–52.
- Yu M, Dilek Y, Yumul Jr GP, Yan Y, Dimalanta CB and Huang CY** (2020) Slab-controlled elemental-isotopic enrichments during subduction initiation magmatism and variations in forearc chemostratigraphy. *Earth and Planetary Science Letters* **538**, 116217.
- Zhou MF, Robinson PT, Malpas J, Edwards SJ and Qi L** (2005) REE and PGE geochemical constraints on the formation of dunites in the Luobusa ophiolite, Southern Tibet. *Journal of Petrology* **46**, 615–39.